Journal of Computational Physics **181,** 98–125 (2002)
doi:10.1006/jcph.2002.7121

Outflow Boundary Conditions for the Fourier Transformed Two-Dimensional Vlasov Equation

Bengt Eliasson

Department of Scientific Computing, Uppsala University, P.O. Box 120, SE-752 37 Uppsala, Sweden; and Department of Astronomy and Space Physics, Uppsala University, Box 515, SE-751 21 Uppsala, Sweden
E-mail: be@tdb.uu.se and be@irfu.se

Received February 21, 2002; revised June 3, 2002

In order to facilitate numerical simulations of plasma phenomena where kinetic processes are important, we have studied the technique of Fourier transforming the Vlasov equation analytically in velocity space, and solving the resulting equation numerically. Particular attention has been paid to the boundary conditions of the Fourier transformed system. By using outgoing wave boundary conditions in the Fourier transformed space, small-scale information in velocity space is carried outside the computational domain and is removed, representing a dissipative loss mechanism. Thereby the so-called recurrence phenomenon is reduced. In the present article, a previously developed method in one spatial and one velocity dimension plus time is generalised to two spatial and two velocity dimensions plus time. Different high-order methods are used for computing derivatives as well as for the time stepping.

Key Words: Vlasov equation; Fourier method; outflow boundary.

1. INTRODUCTION

For many decades, methods of solving numerically the Vlasov equation have been developed, including methods based on Hermite and Fourier expansions [1, 6] and methods based on the time-splitting scheme [4], which has been generalised to higher dimensions for simulations of magnetised plasma [3]. Convective schemes have also been developed for the collisional Boltzmann equation [8], and a conservative scheme has been developed for the one-dimensional Vlasov equation [9].

A problem with the solution of the Vlasov equation is its tendency to become oscillatory in velocity space, due to free-streaming terms. Steep gradients are then created and problems of calculating the v (velocity) derivative of the function accurately increase with time [1, 7]; according to the sampling (Nyqvist) theorem, it will eventually be impossible to represent all parts of the solution on a uniform grid. If not treated carefully, this problem may lead

0021-9991/02 $35.00

to the so-called *recurrence phenomenon*, where parts of the initial condition artificially reappear on the numerical grid [4].

In applications, the recurrence phenomenon may in some cases be unimportant if other processes dominate [15]. It can be important if, for example, the long-time behaviour of a single wave is studied [16]. (In the last reference, the author carefully stopped the simulation before the recurrence phenomenon could take place.)

Several approaches to minimising effects due to the recurrence phenomenon have been developed: A time-splitting scheme has been developed where smoothing operators are applied to the numerical solution so that the finest structures are damped out and never appear on the numerical grid [4]. A Fourier–Fourier method, where the Vlasov equation is Fourier transformed both in $\mathbf{x}$ and $\mathbf{v}$ space, has been developed [1]. A filtered method based on a convolution by a Gaussian function in velocity space has been developed for the Fourier–Fourier method [12], and for the time-split Fourier–Fourier method [11]. In the filtered method, the Vlasov equation is transformed into an equation with smoother solutions.

The method developed in the present paper is related to the above methods, particularly to the Fourier–Fourier method. The Vlasov equation is Fourier transformed in $\mathbf{v}$ space, but *not* in $\mathbf{x}$ space, into an equation with smoother solutions in velocity space, and the small-scale information in velocity space is removed through an outgoing wave boundary condition in the Fourier transformed velocity space. The method was earlier developed for the one-dimensional Vlasov–Poisson system [7] and in the present article is generalised to the two-dimensional Vlasov equation. The main results are the proof of the well-posedness of the Fourier transformed system, including the boundary conditions, and an example of a stable and accurate algorithm which has been implemented to integrate the equation in time.

The method is designed for investigating basic nonlinear particle-wave interactions in magnetised plasma, for example upper hybrid turbulence (and lower hybrid turbulence if ions are allowed to move), and nonlinear coupling to Bernstein modes. Many such interactions are not fully understood and are believed to be the source of some unexplained phenomena observed in experiments [14].

In Section 2.1 the three-dimensional Vlasov–Maxwell system is discussed, together with the Fourier transform technique in velocity space. The two-dimensional Vlasov equation is discussed in Sections 2.2–2.6, where well-posed boundary conditions are derived in preparation for the numerical simulation of the Fourier transformed system. The numerical schemes used to approximate the time-dependent solution of the Vlasov equation system are described in Section 3, and the numerical experiments and results are presented in Section 4, where the results are compared with known theory. In Section 5 some conclusions are drawn regarding the usefulness of the method.

2. THE VLASOV–MAXWELL SYSTEM

2.1. *The Three-Dimensional System*

The Vlasov equation

$$\frac{\partial f_\alpha}{\partial t} + \mathbf{v} \cdot \nabla_{\mathbf{x}} f_\alpha + \frac{q_\alpha}{m_\alpha}(\mathbf{E} + \mathbf{v} \times \mathbf{B}) \cdot \nabla_{\mathbf{v}} f_\alpha = 0 \tag{1}$$

describes the action of the electromagnetic field on charged particles of type α (e.g., "electrons" or "singly ionised oxygen ions"), with each particle having the electric charge q_α and mass m_α. One equation is needed for each species of particles.

The charge and current densities act as sources of self-consistent electromagnetic fields according to the Maxwell equations

$$\nabla_{\mathbf{x}} \cdot \mathbf{E} = \frac{1}{\varepsilon_0} \sum_\alpha q_\alpha n_\alpha, \quad \nabla_{\mathbf{x}} \cdot \mathbf{B} = 0, \tag{2}$$

$$\nabla_{\mathbf{x}} \times \mathbf{E} = -\frac{\partial \mathbf{B}}{\partial t}, \quad \nabla_{\mathbf{x}} \times \mathbf{B} = \mu_0 \sum_\alpha q_\alpha n_\alpha \mathbf{v}_\alpha + \varepsilon_0 \mu_0 \frac{\partial \mathbf{E}}{\partial t}, \tag{3}$$

where the particle number densities n_α and mean velocities $\mathbf{v}_\alpha$ are obtained as moments of the distribution function as

$$n_\alpha(\mathbf{x}, t) = \int_{-\infty}^{\infty} f_\alpha(\mathbf{x}, \mathbf{v}, t)\, \mathrm{d}^3 v, \quad \mathbf{v}_\alpha(\mathbf{x}, t) = \frac{1}{n_\alpha(\mathbf{x}, t)} \int_{-\infty}^{\infty} \mathbf{v} f_\alpha(\mathbf{x}, \mathbf{v}, t)\, \mathrm{d}^3 v, \tag{4}$$

respectively. The Vlasov equations together with the Maxwell equations form a closed system.

By using the Fourier transform pair

$$f_\alpha(\mathbf{x}, \mathbf{v}, t) = \int_{-\infty}^{\infty} \hat{f}_\alpha(\mathbf{x}, \boldsymbol{\eta}, t) e^{-\mathrm{i}\eta \cdot \mathbf{v}}\, \mathrm{d}^3 \eta, \tag{5}$$

$$\hat{f}_\alpha(\mathbf{x}, \boldsymbol{\eta}, t) = \frac{1}{(2\pi)^3} \int_{-\infty}^{\infty} f_\alpha(\mathbf{x}, \mathbf{v}, t) e^{\mathrm{i}\eta \cdot \mathbf{v}}\, \mathrm{d}^3 v, \tag{6}$$

the velocity variable $\mathbf{v}$ is transformed into a new variable $\boldsymbol{\eta}$ and the unknown function $f(\mathbf{x}, \mathbf{v}, t)$ is changed to a new, complex valued function $\hat{f}(\mathbf{x}, \boldsymbol{\eta}, t)$, which obeys the transformed Vlasov equation

$$\frac{\partial \hat{f}_\alpha}{\partial t} - \mathrm{i} \nabla_{\mathbf{x}} \cdot \nabla_\eta \hat{f}_\alpha - \frac{q_\alpha}{m_\alpha} \{\mathrm{i} \mathbf{E} \cdot \boldsymbol{\eta} \hat{f}_\alpha + \nabla_\eta \cdot [(\mathbf{B} \times \boldsymbol{\eta}) \hat{f}_\alpha]\} = 0. \tag{7}$$

The nabla operators $\nabla_{\mathbf{x}}$ and $\nabla_{\boldsymbol{\eta}}$ denote differentiation with respect to $\mathbf{x}$ and $\boldsymbol{\eta}$, respectively.

Equation (7) is again solved together with the Maxwell equations, where the particle number densities and mean velocities are obtained as

$$n_\alpha(\mathbf{x}, t) = (2\pi)^3 \hat{f}_\alpha(\mathbf{x}, \mathbf{0}, t), \quad \mathbf{v}_\alpha(\mathbf{x}, t) = -\mathrm{i} \frac{(2\pi)^3}{n_\alpha(\mathbf{x}, t)} [\nabla_\eta \hat{f}_\alpha(\mathbf{x}, \boldsymbol{\eta}, t)]_{\eta=0}, \tag{8}$$

respectively. One can note that the integrals over infinite $\mathbf{v}$ space have been converted to evaluations in $\boldsymbol{\eta}$ space. The factor $(2\pi)^3$ in Eqs. (6) and (8) is valid for three velocity dimensions. For n velocity dimensions the factor is $(2\pi)^n$.

2.2. *The Two-Dimensional Vlasov–Poisson System*

We have chosen to study numerically the two-dimensional Vlasov–Poisson system consisting of electrons and ions, with the ions assumed to be fixed uniformly in space. We

assume an external magnetic field $\mathbf{B}(x_1, x_2, t)$ to be directed in the x_3 direction, perpendicularly to the motion of the electrons moving in the (x_1, x_2) plane. The electric field is calculated self-consistently, using an electrostatic approximation. These assumptions lead to the system

$$\frac{\partial f}{\partial t} + v_1 \frac{\partial f}{\partial x_1} + v_2 \frac{\partial f}{\partial x_2} - \frac{e}{m}\left(E_1 \frac{\partial f}{\partial v_1} + E_2 \frac{\partial f}{\partial v_2} + B v_2 \frac{\partial f}{\partial v_1} - B v_1 \frac{\partial f}{\partial v_2} \right) = 0, \tag{9}$$

$$E_1(x_1, x_2, t) = -\frac{\partial}{\partial x_1}\Phi(x_1, x_2, t), \quad E_2(x_1, x_2, t) = -\frac{\partial}{\partial x_2}\Phi(x_1, x_2, t), \tag{10}$$

$$-\left(\frac{\partial^2 \Phi}{\partial x_1^2} + \frac{\partial^2 \Phi}{\partial x_2^2} \right) = \frac{e}{\varepsilon_0}\left[n_0 - \int_{-\infty}^{\infty}\int_{-\infty}^{\infty} f(x_1, x_2, v_1, v_2, t)\, \mathrm{d}v_1\, \mathrm{d}v_2 \right], \tag{11}$$

where n_0 is the neutralising heavy-ion-density background.

By using the Fourier transform pair

$$\begin{aligned} f(x_1, x_2, v_1, v_2, t) &= \int_{-\infty}^{\infty}\int_{-\infty}^{\infty} \hat{f}(x_1, x_2, \eta_1, \eta_2, t) e^{-\mathrm{i}(\eta_1 v_1 + \eta_2 v_2)}\, \mathrm{d}\eta_2\, \mathrm{d}\eta_1, \\ \hat{f}(x_1, x_2, \eta_1, \eta_2, t) &= \frac{1}{(2\pi)^2}\int_{-\infty}^{\infty}\int_{-\infty}^{\infty} f(x_1, x_2, v_1, v_2, t) e^{\mathrm{i}(\eta_1 v_1 + \eta_2 v_2)}\, \mathrm{d}v_2\, \mathrm{d}v_1, \end{aligned} \tag{12}$$

the system (9)–(11) is transformed into

$$\frac{\partial \hat{f}}{\partial t} - \mathrm{i}\frac{\partial^2 \hat{f}}{\partial x_1 \partial \eta_1} - \mathrm{i}\frac{\partial^2 \hat{f}}{\partial x_2 \partial \eta_2} + \frac{e}{m}\left[\mathrm{i}(E_1\eta_1 + E_2\eta_2)\hat{f} + B\eta_1 \frac{\partial \hat{f}}{\partial \eta_2} - B\eta_2 \frac{\partial \hat{f}}{\partial \eta_1} \right] = 0, \tag{13}$$

$$E_1(x_1, x_2, t) = -\frac{\partial}{\partial x_1}\Phi(x_1, x_2, t), \quad E_2(x_1, x_2, t) = -\frac{\partial}{\partial x_2}\Phi(x_1, x_2, t), \tag{14}$$

$$-\left(\frac{\partial^2 \Phi}{\partial x_1^2} + \frac{\partial^2 \Phi}{\partial x_2^2} \right) = \frac{e}{\varepsilon_0}\left[n_0 - (2\pi)^2 \hat{f}(x_1, x_2, \eta_1, \eta_2, t)_{\eta_1 = \eta_2 = 0} \right]. \tag{15}$$

The Fourier transformed Vlasov equation was earlier studied analytically by Neunzert [17, 18].

The systems (9)–(11) and (13)–(15) can be cast into dimensionless form by a scaling of variables: The time t is scaled to the inverse of the plasma frequency $\omega_\mathrm{p}^{-1} = \sqrt{\varepsilon_0 m/(n_0 e^2)}$, the velocity v is scaled to the thermal velocity $v_\mathrm{th} = \sqrt{k_\mathrm{B} T/m}$, the new variables η_1 and η_2 are scaled to the inverse of the thermal velocity, and the spatial variables x_1 and x_2 are scaled to the Debye length $r_\mathrm{D} = v_\mathrm{th}\omega_\mathrm{p}^{-1}$. Finally, the function $\hat{f}$ is scaled to the background density n_0, the function f is scaled to $n_0 v_\mathrm{th}^{-2}$, the electric field E is scaled to the quantity $v_\mathrm{th}^2 r_\mathrm{D}^{-1}(m/e)$, and the electric potential Φ is scaled to $v_\mathrm{th}^2(m/e)$. In terms of primed, dimensionless variables, the scaling is

$$t = \omega_\mathrm{p}^{-1} t', \quad \mathbf{v} = v_\mathrm{th}\mathbf{v}', \quad \mathbf{x} = r_\mathrm{D}\mathbf{x}', \tag{16}$$

$$\boldsymbol{\eta} = v_\mathrm{th}^{-1}\boldsymbol{\eta}', \quad \hat{f} = n_0 \hat{f}, \quad f = n_0 v_\mathrm{th}^{-2} f', \tag{17}$$

$$\mathbf{E} = v_\mathrm{th}^2 r_\mathrm{D}^{-1}(m/e)\mathbf{E}', \quad \Phi = v_\mathrm{th}^2(m/e)\Phi', \quad \mathbf{B} = \omega_\mathrm{p}(m/e)\mathbf{B}. \tag{18}$$

By this scaling of variables, and omitting the primes, the systems (9)–(11) and (13)–(15)

attain the dimensionless form

$$\frac{\partial f}{\partial t} + v_1 \frac{\partial f}{\partial x_1} + v_2 \frac{\partial f}{\partial x_2} - \left(E_1 \frac{\partial f}{\partial v_1} + E_2 \frac{\partial f}{\partial v_2} + B v_2 \frac{\partial f}{\partial v_1} - B v_1 \frac{\partial f}{\partial v_2} \right) = 0, \tag{19}$$

$$E_1 = -\frac{\partial \Phi}{\partial x_1}, \quad E_2 = -\frac{\partial \Phi}{\partial x_2}, \tag{20}$$

$$-\left(\frac{\partial^2 \Phi}{\partial x_1^2} + \frac{\partial^2 \Phi}{\partial x_2^2} \right) = 1 - \int_{-\infty}^{\infty} \int_{-\infty}^{\infty} f \, \mathrm{d}v_1 \, \mathrm{d}v_2 \tag{21}$$

and

$$\frac{\partial \hat{f}}{\partial t} - \mathrm{i} \frac{\partial^2 \hat{f}}{\partial x_1 \partial \eta_1} - \mathrm{i} \frac{\partial^2 \hat{f}}{\partial x_2 \partial \eta_2} + \mathrm{i}(E_1 \eta_1 + E_2 \eta_2) \hat{f} + B \eta_1 \frac{\partial \hat{f}}{\partial \eta_2} - B \eta_2 \frac{\partial \hat{f}}{\partial \eta_1} = 0, \tag{22}$$

$$E_1 = -\frac{\partial \Phi}{\partial x_1}, \quad E_2 = -\frac{\partial \Phi}{\partial x_2}, \tag{23}$$

$$-\left(\frac{\partial^2 \Phi}{\partial x_1^2} + \frac{\partial^2 \Phi}{\partial x_2^2} \right) = 1 - (2\pi)^2 (\hat{f})_{\eta_1 = \eta_2 = 0}, \tag{24}$$

respectively.

2.3. *The Problem of Oscillatory Structures in Velocity Space*

We here repeat the motivation [1, 4, 7] for solving numerically the Fourier transformed Vlasov–Poisson system (22)–(24) in $(\mathbf{x}, \boldsymbol{\eta}, t)$ space instead of solving the original system (19)–(21) in $(\mathbf{x}, \mathbf{v}, t)$ space.

Due to free-streaming terms, the Vlasov equation may develop oscillatory structures in velocity space. This can be illustrated by studying the interaction-free one-dimensional equation

$$\frac{\partial f}{\partial t} + v \frac{\partial f}{\partial x} = 0 \tag{25}$$

with the initial condition

$$f(x, v, 0) = f_0(x, v) = [1 + A \cos(k_x x)] e^{-v^2/2}. \tag{26}$$

The solution to this initial value problem is

$$f(x, v, t) = f_0(x - vt, v) = [1 + A \cos(k_x x - k_x v t)] e^{-v^2/2}. \tag{27}$$

Solution (27) becomes increasingly oscillatory with respect to the velocity v as the time t increases, due to the $k_x v t$ term inside the cosine function. It will finally be impossible to represent the solution on a grid in (x, v) space according to the sampling (Nyqvist) theorem, which states that one needs more than two grid points per wavelength in order to represent a solution on an equidistant grid.

For the example given above, it is easy to calculate the time after which the solution violates the sampling theorem: If one assumes that the grid size in v direction is Δv, with function values sampled for $v = 0, \pm\Delta v, \pm 2\Delta v, \ldots, \pm N_v \Delta v$, then the sampling theorem

states the condition $\lambda_v/\Delta v > 2$ for representing the solution, where λ_v is the "wavelength" of the solution. The $k_x vt$ term in Eq. (27) gives the wavelength of the cosine function as $\lambda_v = 2\pi/k_x t$ in the velocity direction, which gives the condition $t < \pi/k_x \Delta v$ for the times when it is possible to represent the solution on the computational grid. After this time the solution violates the sampling theorem and it will therefore be impossible to represent the solution on the grid.

The *recurrence phenomenon* [4] occurs at time $t = T_R = 2\pi/k_x \Delta v$, which is the time for the values of the initial condition to artificially reappear on the numerical grid, a numerical effect caused by the violation of the sampling theorem just described.

2.4. *Some Properties of the Fourier Transformed System*

For most of the physical problems, the distribution function $f(\mathbf{x}, \mathbf{v}, t)$ vanishes as a Gaussian function $\sim\exp(-\alpha v^2)$ for large values of v. This behaviour guarantees that the Fourier transformed function $\hat{f}(\mathbf{x}, \boldsymbol{\eta}, t)$ will be a smooth function of $\boldsymbol{\eta}$ and that all $\boldsymbol{\eta}$ derivatives therefore will be well-defined. This is favourable when the $\boldsymbol{\eta}$ derivatives in Eq. (22) are to be approximated by numerical difference approximations.

The difference in behaviour between the Fourier transformed system and the original system can be illustrated by the example in the previous section; taking the Fourier transform of solution (27) in the velocity space yields

$$\hat{f}(x, \eta, t) = \frac{1}{\sqrt{2\pi}} \left\{ e^{-\eta^2/2} + \frac{A}{2} \left[\cos(k_x x) \left(e^{-(\eta - k_x t)^2/2} + e^{-(\eta + k_x t)^2/2} \right) + \mathrm{i} \sin(k_x x) \left(e^{-(\eta - k_x t)^2/2} - e^{-(\eta + k_x t)^2/2} \right) \right] \right\}. \tag{28}$$

This function does *not* become oscillatory for large times. The $\exp[-(\eta - k_x t)^2/2]$ and $\exp[-(\eta + k_x t)^2/2]$ terms represent smooth wave packets which move away from the origin $\eta = 0$ as t increases. Instead of becoming *oscillatory*, the Fourier transformed solution becomes *wider* in η space with increasing time.

A symmetry property [1] exists for $\hat{f}(\mathbf{x}, \boldsymbol{\eta}, t)$: Since the original distribution function $f(\mathbf{x}, \mathbf{v}, t)$ is real valued, the Fourier transformed function $\hat{f}(x_1, x_2, \eta_1, \eta_2, t)$ fulfills the relation

$$\hat{f}(x_1, x_2, -\eta_1, -\eta_2, t) = [\hat{f}(x_1, x_2, \eta_1, \eta_2, t)]^*, \tag{29}$$

where $*$ denotes complex conjugation. We will therefore later restrict the problem to only nonnegative η_1, and we will obtain the values for negative η_1, when needed, by the symmetry (29) (see the numerical approach in Section 3). For the derivatives, it holds that for even numbers of derivatives of the function $\hat{f}$ with respect to (η_1, η_2), the real part is even and the imaginary part is odd. For odd numbers of derivatives of $\hat{f}$, the opposite holds.

2.5. *Invariants of the Vlasov–Poisson System*

The two-dimensional system (19)–(21) has several conserved (time independent) quantities, such as the energy norm

$$\|f\|^2 = \int_0^{L_1} \int_0^{L_2} \int_{-\infty}^{\infty} \int_{-\infty}^{\infty} f^2 \, \mathrm{d}v_2 \, \mathrm{d}v_1 \, \mathrm{d}x_2 \, \mathrm{d}x_1 \tag{30}$$

and the total number of particles

$$N = \int_0^{L_1} \int_0^{L_2} \int_{-\infty}^{\infty} \int_{-\infty}^{\infty} f \, \mathrm{d}v_2 \, \mathrm{d}v_1 \, \mathrm{d}x_2 \, \mathrm{d}x_1. \tag{31}$$

If $B = 0$, then the total linear momentum

$$\mathbf{p} = \int_0^{L_1} \int_0^{L_2} \int_{-\infty}^{\infty} \int_{-\infty}^{\infty} (\hat{x}_1 v_1 + \hat{x}_2 v_2) f \, \mathrm{d}v_2 \, \mathrm{d}v_1 \, \mathrm{d}x_2 \, \mathrm{d}x_1 \tag{32}$$

is conserved, and if B is independent of t, then the total energy (the Hamiltonian)

$$W = \int_0^{L_1} \int_0^{L_2} \left[\int_{-\infty}^{\infty} \int_{-\infty}^{\infty} \frac{1}{2}\left(v_1^2 + v_2^2\right) f \, \mathrm{d}v_2 \, \mathrm{d}v_1 + \frac{1}{2}\left(E_1^2 + E_1^2\right) \right] \mathrm{d}x_2 \, \mathrm{d}x_1 \tag{33}$$

is conserved.

There exist many entropylike conserved functionals similar to $\|f\|^2$, such as where f^2 is replaced by $f \log(f)$ [16]. The norm $\|f\|$ has its counterpart in the Fourier transformed space via the Parseval relation, and is also important in the definition of well-posed problems [20].

The corresponding invariants for the Fourier transformed system (22)–(24) are

$$\|\hat{f}\|^2 = \int_0^{L_1} \int_0^{L_2} \int_{-\infty}^{\infty} \int_{-\infty}^{\infty} |\hat{f}|^2 \, \mathrm{d}\eta_2 \, \mathrm{d}\eta_2 \, \mathrm{d}x_2 \, \mathrm{d}x_1, \tag{34}$$

where a factor $1/(2\pi)^2$ has been omitted, and

$$N = \int_0^{L_1} \int_0^{L_2} (2\pi)^2 (\hat{f})_{\eta_1=\eta_2=0} \, \mathrm{d}x_2 \, \mathrm{d}x_1, \tag{35}$$

$$\mathbf{p} = \int_0^{L_1} \int_0^{L_2} -\mathrm{i}(2\pi)^2 \left[\hat{x}_1 \frac{\partial \hat{f}}{\partial \eta_1} + \hat{x}_2 \frac{\partial \hat{f}}{\partial \eta_2} \right]_{\eta_1=\eta_2=0} \mathrm{d}x_2 \, \mathrm{d}x_1, \tag{36}$$

$$W = \int_0^{L_1} \int_0^{L_2} \left\{ -\frac{1}{2}(2\pi)^2 \left[\frac{\partial^2 \hat{f}}{\partial \eta_1^2} + \frac{\partial^2 \hat{f}}{\partial \eta_2^2} \right]_{\eta_1=\eta_2=0} + \frac{1}{2}\left(E_1^2 + E_2^2\right) \right\} \mathrm{d}x_2 \, \mathrm{d}x_1, \tag{37}$$

respectively. In the absence of analytical "calibration" solutions for nonlinear problems, it is important to check how well a numerical scheme conserves these invariants. When the system is restricted to a bounded domain, the norm $\|\hat{f}\|^2$ will be a nonincreasing, positive function of time (see below), while the other three quantities will still be conserved.

2.6. *Restriction to a Bounded Domain*

In order to adapt the system (22)–(24) for numerical simulations, it must be restricted to a bounded domain and rewritten in a new form.

The computational domain is restricted to $0 \le x_1 < L_1$, $0 \le x_2 < L_2$, $0 \le \eta_1 \le \eta_{1,\max}$, and $-\eta_{2,\max} \le \eta_2 \le \eta_{2,\max}$. For negative η_1, the symmetry (29) is used to obtain function values; it is therefore not necessary to numerically represent the solution for negative η_1.

Furthermore, at the boundary $\eta_1 = 0$, function values for negative η_2 can again be obtained by the symmetry relation (29).

In the x_1 and x_2 directions, the periodic boundary conditions

$$\hat{f}(x_1 + L_1, x_2, \eta_1, \eta_2, t) = \hat{f}(x_1, x_2, \eta_1, \eta_2, t), \tag{38}$$

$$\hat{f}(x_1, x_2 + L_1, \eta_1, \eta_2, t) = \hat{f}(x_1, x_2, \eta_1, \eta_2, t), \tag{39}$$

respectively, are used.

The artificial boundaries at $\eta_1 = \eta_{1,\max}$ and $\eta_2 = \pm\eta_{2,\max}$ must be treated with care so that they do not give rise to reflections of waves or to instabilities. The strategy is to let outgoing waves pass over the boundaries, and to set incoming waves to zero. The problem of separating outgoing waves from incoming waves is solved by employing the spatial Fourier series expansions (transforms). In order to explore the idea, one can study the reduced initial value problem with a constant magnetic field $B = B_0$ [cf. Eq. (22)],

$$\frac{\partial \hat{f}}{\partial t} - \mathrm{i}\frac{\partial^2 \hat{f}}{\partial x_1 \partial \eta_1} - \mathrm{i}\frac{\partial^2 \hat{f}}{\partial x_2 \partial \eta_2} + B_0 \eta_1 \frac{\partial \hat{f}}{\partial \eta_2} - B_0 \eta_2 \frac{\partial \hat{f}}{\partial \eta_1} = 0, \tag{40}$$

$$f(x_1, x_2, \eta_1, \eta_2, 0) = f_0(x_1, x_2, \eta_1, \eta_2). \tag{41}$$

By introducing the spatial Fourier series pairs in x_1 and x_2 space,

$$\tilde{\phi}_{1,i_1} = \mathrm{F}_1 \phi_1 = \frac{1}{L_1} \int_0^{L_1} \phi_1(x_1) e^{-\mathrm{i}k_{x_1} x_1} \, \mathrm{d}x_1, \tag{42}$$

$$\phi_1 = \mathrm{F}_1^{-1} \tilde{\phi}_1 = \sum_{i_1=-\infty}^{\infty} \tilde{\phi}_{1,i_1} e^{\mathrm{i}k_{x_1} x_1}, \tag{43}$$

$$k_{x_1} = \frac{2\pi i_1}{L_1}, \quad i_1 = 0, \pm 1, \pm 2, \ldots. \tag{44}$$

and

$$\tilde{\phi}_{2,i_2} = \mathrm{F}_2 \phi_2 = \frac{1}{L_2} \int_0^{L_2} \phi_2(x_2) e^{-\mathrm{i}k_{x_2} x_2} \, \mathrm{d}x_2 \tag{45}$$

$$\phi_2 = \mathrm{F}_2^{-1} \tilde{\phi}_2 = \sum_{i_2=-\infty}^{\infty} \tilde{\phi}_{2,i_2} e^{\mathrm{i}k_{x_2} x_2} \tag{46}$$

$$k_{x_2} = \frac{2\pi i_2}{L_2}, \quad i_2 = 0, \pm 1, \pm 2, \ldots, \tag{47}$$

respectively, and Fourier transforming Eq. (40) in the x_1 and x_2 directions, one obtains a new differential equation for the unknown function $\hat{f}(k_{x_1}, k_{x_2}, \eta_1, \eta_2, t)$,

$$\frac{\partial \tilde{f}}{\partial t} + \left(k_{x_1} - B_0 \eta_2\right) \frac{\partial \tilde{f}}{\partial \eta_1} + \left(k_{x_2} + B_0 \eta_1\right) \frac{\partial \tilde{f}}{\partial \eta_2} = 0, \tag{48}$$

$$\tilde{f}\left(k_{x_1}, k_{x_2}, \eta_1, \eta_2, t\right)_{t=0} = \tilde{f}_0\left(k_{x_1}, k_{x_2}, \eta_1, \eta_2\right). \tag{49}$$

This is a hyperbolic equation for which the intial values are transported along the characteristic curves, given by

$$\frac{\mathrm{d}\eta_1(t)}{\mathrm{d}t} = k_{x_1} - B_0\eta_2(t), \tag{50}$$

$$\frac{\mathrm{d}\eta_2(t)}{\mathrm{d}t} = k_{x_2} - B_0\eta_1(t). \tag{51}$$

Along the boundary $\eta_1 = \eta_{1,\max}$, Eq. (50) describes an *outflow* of data when $k_{x_1} - B_0\eta_2 \geq 0$ and an *inflow* of data when $k_{x_1} - B_0\eta_2 < 0$. A well-posed boundary condition is to set the inflow to zero at the boundary, i.e.,

$$\tilde{f}_{\eta_1=\eta_{1,\max}} = 0, \quad k_{x_1} - B_0\eta_2 < 0, \tag{52}$$

which can be expressed with the help of the Heaviside step function H as

$$\tilde{f} = H\big(k_{x_1} - B_0\eta_2\big)\tilde{f}, \quad \eta_1 = \eta_{1,\max}, \tag{53}$$

where

$$H\big(k_{x_1} - B_0\eta_2\big) = \begin{cases} 1, & k_{x_1} - B_0\eta_2 \geq 0, \\ 0, & k_{x_1} - B_0\eta_2 < 0. \end{cases} \tag{54}$$

The boundary condition (53) allows outgoing waves to pass over the boundary and to be removed, while incoming waves are set to zero; the removal of the outgoing waves corresponds to the losing of information about the finest structures in velocity space.

Inverse Fourier transforming Eq. (53) then gives the boundary condition for the original problem (40) as

$$\hat{f} = \mathrm{F}_1^{-1} H\big(k_{x_1} - B_0\eta_2\big)\mathrm{F}_1\hat{f}, \quad \eta_1 = \eta_{1,\max}. \tag{55}$$

The operator $\mathrm{F}_1^{-1}H(k_{x_1} - B_0\eta_2)\mathrm{F}_1$ is a projection operator which removes incoming waves at the boundary $\eta_1 = \eta_{1,\max}$. Similarly, the boundary conditions at $\eta_2 = \pm\eta_{2,\max}$ become

$$\hat{f} = \mathrm{F}_2^{-1} H\big(k_{x_2} + B_0\eta_1\big)\mathrm{F}_2\hat{f}, \quad \eta_2 = \eta_{2,\max} \tag{56}$$

and

$$\hat{f} = \mathrm{F}_2^{-1} H\big(-k_{x_2} - B_0\eta_1\big)\mathrm{F}_2\hat{f}, \quad \eta_2 = -\eta_{2,\max}. \tag{57}$$

In order to find well-posed boundary conditions in the η_1 and η_2 directions in the case when $B = B(x_1, x_2, t)$ varies both in time t and in x_1 and x_2 space, Eq. (22) is rewritten in the equivalent form

$$\begin{aligned} &\frac{\partial\hat{f}}{\partial t} - \mathrm{i}\exp\left[\mathrm{i}\eta_2\int_0^{x_1}(B - B_{01})\,\mathrm{d}x_1\right]\frac{\partial}{\partial\eta_1}\left(-\mathrm{i}\eta_2 B_{01} + \frac{\partial}{\partial x_1}\right)G_1 \\ &\quad - \mathrm{i}\exp\left[-\mathrm{i}\eta_1\int_0^{x_2}(B - B_{02})\,\mathrm{d}x_2\right]\frac{\partial}{\partial\eta_2}\left(\mathrm{i}\eta_1 B_{02} + \frac{\partial}{\partial x_2}\right)G_2 \\ &\quad + \mathrm{i}(E_1\eta_1 + E_2\eta_2)\hat{f} = 0, \end{aligned} \tag{58}$$

where the functions

$$G_1 = \hat{f} \exp\left[-i\eta_2 \int_0^{x_1} (B - B_{01})\, dx_1\right] \tag{59}$$

and

$$G_2 = \hat{f} \exp\left[i\eta_1 \int_0^{x_2} (B - B_{02})\, dx_2\right] \tag{60}$$

and the averaged magnetic fields are

$$B_{01}(x_2, t) = \frac{1}{L_1} \int_0^{L_1} B\, dx_1 \tag{61}$$

and

$$B_{02}(x_1, t) = \frac{1}{L_2} \int_0^{L_2} B\, dx_2. \tag{62}$$

The form (58) of the Vlasov equation makes it possible to introduce stable numerical boundary conditions in the η_1 and η_2 directions in a systematic manner, as will be shown in Section 3.2. One also notes that $\int_0^{x_1}(B - B_{01})\, dx_1$ and $\int_0^{x_2}(B - B_{02})\, dx_2$ are periodic functions in x_1 and x_2 space; this is the reason for the introduction of B_{01} and B_{02}, respectively.

By studying the flow of data in the η_1 and η_2 directions for the auxiliary functions G_1 and G_2, respectively, one finds the outflow boundary conditions to be

$$G_1 = \mathrm{F}_1^{-1} H\left(k_{x_1} - \eta_2 B_{01}\right) \mathrm{F}_1 G_1, \qquad \eta_1 = \eta_{1,\max}, \tag{63}$$

$$G_2 = \mathrm{F}_2^{-1} H\left(k_{x_2} - \eta_1 B_{02}\right) \mathrm{F}_2 G_2, \qquad \eta_2 = \eta_{2,\max}, \tag{64}$$

$$G_2 = \mathrm{F}_2^{-1} H\left(-k_{x_2} - \eta_1 B_{02}\right) \mathrm{F}_2 G_2, \quad \eta_2 = -\eta_{2,\max}. \tag{65}$$

In the case when B is independent of x_1 and x_2, the boundary conditions (63)–(65) reduce to the conditions (55)–(57). In the case where the domain is extended to negative η_1, there will be a boundary condition

$$G_1 = \mathrm{F}_1^{-1} H\left(-k_{x_1} + \eta_2 B_{01}\right) \mathrm{F}_1 G_1, \quad \eta_1 = -\eta_{1,\max}, \tag{66}$$

which will be used in the numerical scheme (see Section 3.2). Using Eqs. (59) and (60) in Eqs. (63)–(66) yields the boundary conditions for $\hat{f}$.

A proof of the well-posedness of the continuous problem with the given boundary conditions is given in the Appendix.

3. THE NUMERICAL APPROACH

3.1. *Discretisation*

We discretise the problem on a rectangular, equidistant grid with periodic boundary conditions in the x_1 and x_2 directions. In the η_1 direction the grid begins at $\eta_1 = 0$ and ends at $\eta_1 = \eta_{1,\max}$, and in the η_2 direction the grid begins at $\eta_2 = -\eta_{2,\max}$ and ends at $\eta_2 = \eta_{2,\max}$.

The approximate function values at the grid points are enumerated such that

$$\hat{f}\left(x_{1,i_1}, x_{2,i_2}, \eta_{1,j_1}, \eta_{2,j_2}, t_k\right) \approx \hat{f}^k_{i_1,i_2,j_1,j_2}, \quad \Phi\left(x_{1,i_1}, x_{2,i_2}, t_k\right) \approx \Phi^k_{i_1,i_2}, \tag{67}$$

$$E_1\left(x_{1,i_1}, x_{2,i_2}, t_k\right) \approx E^k_{1,i_1,i_2}, \qquad E_2\left(x_{1,i_1}, x_{2,i_2}, t_k\right) \approx E^k_{2,i_1,i_2}, \tag{68}$$

with the known variables discretised as

$$x_{1,i_1} = i_1 \Delta x_1, \qquad i_1 = 0, 1, \ldots, N_{x_1} - 1, \tag{69}$$

$$x_{2,i_2} = i_2 \Delta x_2, \qquad i_2 = 0, 1, \ldots, N_{x_2} - 1, \tag{70}$$

$$\eta_{1,j_1} = j_1 \Delta \eta_1, \qquad j_1 = 0, 1, \ldots, N_{\eta_1}, \tag{71}$$

$$\eta_{2,j_2} = j_2 \Delta \eta_2, \qquad j_2 = -N_{\eta_2} \ldots -1, 0, 1, \ldots, N_{\eta_2}, \tag{72}$$

$$t_k = t_{k-1} + \Delta t_k, t_0 = 0, \quad k = 1, 2, \ldots, N_t, \tag{73}$$

and with the grid sizes calculated as

$$\Delta x_1 = \frac{L_1}{N_{x_1}}, \quad \Delta x_2 = \frac{L_2}{N_{x_2}}, \quad \Delta \eta_1 = \frac{\eta_{1,\max}}{N_{\eta_1}}, \quad \Delta \eta_2 = \frac{\eta_{2,\max}}{N_{\eta_2}}, \tag{74}$$

respectively. The time step Δt_k is calculated adaptively (see Section 3.3). For convenience, only even numbers will be used for N_{x_1} and N_{x_2}.

3.2. *Numerical Approximations*

The Vlasov–Poisson system (58), (23), and (24) together with the boundary conditions (63)–(66) is approximated by a semidiscretisation in x_1, x_2, η_1, and η_2 space. After that, time steps are taken with the fourth-order Runge–Kutta method.

The Vlasov equation (58) is solved numerically on the domain, including the boundaries at $\eta_1 = \eta_{1,\max}$ and $\eta_2 = \eta_{2,\max}$, after applying the boundary conditions (63)–(66) on $\hat{f}$[via G_1 and G_2; see Eqs. (59) and (60)] in the right-hand side of Eq. (58), and after solving the algebraic Eqs. (23) and (24) numerically to obtain E_1 and E_2; one can view E_1 and E_2 as *functions* of $\hat{f}$. This yields the semidiscretisation

$$\frac{\mathrm{d}}{\mathrm{d}t} \hat{f}_{i_1,i_2,j_1,j_2} = P(\hat{f})_{i_1,i_2,j_1,j_2}, \tag{75}$$

where P is a grid function representing the numerical approximation of the right-hand sides of Eq. (58); the function P is a function of all components $\hat{f}_{i_1,i_2,j_1,j_2}$. The unknowns $\hat{f}_{i_1,i_2,j_1,j_2}$ are then discretised also in *time*, and the time stepping is performed with the Runge–Kutta algorithm (where we omit writing out the subscript $_{i_1,i_2,j_1,j_2}$ on K, P, and $\hat{f}$):

1. $K^{(1)} \leftarrow P(\hat{f}^k), \forall i_1, i_2, j_1, j_2.$
2. $K^{(2)} \leftarrow P(\hat{f}^k + K^{(1)}\Delta t/2), \forall i_1, i_2, j_1, j_2.$
3. $K^{(3)} \leftarrow P(\hat{f}^k + K^{(2)}\Delta t/2), \forall i_1, i_2, j_1, j_2.$
4. $K^{(4)} \leftarrow P(\hat{f}^k + K^{(3)}\Delta t/2), \forall i_1, i_2, j_1, j_2.$
5. $\hat{f}^{k+1} \leftarrow \hat{f}^k + \frac{\Delta t}{6}(K^{(1)} + 2K^{(2)} + 2K^{(3)} + K^{(4)}), \forall i_1, i_2, j_1, j_2.$

The steps needed for obtaining the approximation P_{i_1,i_2,j_1,j_2} are as follows:

1. Apply the boundary conditions (63)–(66) on the present Runge–Kutta stage of $\hat{f}$. In the first Runge–Kutta step, the operators act on $\hat{f}^k$ and the result replaces $\hat{f}^k$ itself.

2. Calculate the electric field numerically from Eqs. (23) and (24) using the present Runge–Kutta stage of $\hat{f}$.

3. Calculate a numerical approximation of Eq. (58) for all points including the points along the boundaries $\eta_1 = \eta_{1,\max}$ and $\eta_2 = \eta_{2,\max}$.

Noting that the solution is periodic in the x_1 and x_2 directions, pseudospectral methods (trigonometric interpolations) are employed to calculate the x_1 and x_2 derivatives and integrals accurately. The Fourier transform and its inverse is approximated by the discrete Fourier transform and inverse discrete Fourier transform, respectively. The discrete transforms are efficiently calculated by using the fast Fourier transform (FFT) and inverse fast Fourier transform (IFFT) algorithms; symbolically, the notations $\mathrm{F}_1 \approx \mathrm{FFT}_1$, $\mathrm{F}_1^{-1} \approx \mathrm{IFFT}_1$ and $\mathrm{F}_2 \approx \mathrm{IFFT}_2$, $\mathrm{F}_2^{-1} \approx \mathrm{IFFT}_2$ will be used.

A problem is that the Fourier components corresponding to $i_1 = \pm N_{x_1}/2$ and $i_2 = \pm N_{x_2}/2$ obtained in the IFFT_1 and FFT_2 algorithms are not well-defined since they correspond exactly to the Nyqvist frequency, and in our numerical experiments they have given rise to numerical instabilities. Therefore these components are set to zero in the approximations of x_1 and x_2 derivatives in Eq. (58); the algorithms are described below.

The approximations of the x_1 and x_2 derivatives are obtained as

$$\frac{\partial \phi}{\partial x_1} \approx \mathrm{IFFT}_1\left[\mathrm{i}k_{x_1}\mathrm{FFT}_1(\phi)\right] \tag{76}$$

and

$$\frac{\partial \phi}{\partial x_2} \approx \mathrm{IFFT}_2\left[\mathrm{i}k_{x_2}\mathrm{FFT}_1(\phi)\right], \tag{77}$$

respectively, where the components of the wavenumbers are $(k_{x_1})_{i_1} = 2\pi i_1/L_1$ with $i_1 = -(N_{x_1}/2-1), \ldots, (N_{x_1}/2)$ and $(k_{x_2})_{i_2} = 2\pi i_2/L_2$ with $i_2 = -(N_{x_2}/2-1), \ldots, (N_{x_2}/2)$, respectively.

The two components of the electric field E_1 and E_2 are integrated numerically from Eqs. (23) and (24) with the approximations (76) and (77) as

$$E_1 \approx \mathrm{IFFT}_2\mathrm{IFFT}_1\left\{\left[\frac{-\mathrm{i}k_{x_1}}{k_{x_1}^2 + k_{x_2}^2}\right]\mathrm{FFT}_2\mathrm{FFT}_1\left[1 - (2\pi)^2 \hat{f}^k_{i_1,i_2,0,0}\right]\right\} \tag{78}$$

and

$$E_2 \approx \mathrm{IFFT}_2\mathrm{IFFT}_1\left\{\left[\frac{-\mathrm{i}k_{x_2}}{k_{x_1}^2 + k_{x_2}^2}\right]\mathrm{FFT}_2\mathrm{FFT}_1\left[1 - (2\pi)^2 \hat{f}^k_{i_1,i_2,0,0}\right]\right\}, \tag{79}$$

respectively; i.e., the expression $[1 - (2\pi)^2 \hat{f}^k_{i_1,i_2,0,0}]$ is Fourier transformed in the x_1 and x_2 direction, then multiplied with the appropriate factors, and then inverse Fourier transformed to obtain E_1 and E_2. The components corresponding to $k_{x_1} = k_{x_2} = 0$ are set to zero.

Similarly, the expressions for the integrated magnetic field used in Eqs. (58)–(60) are approximated, up to "constants" of integration which will have no effect on the numerical

results, by

$$\int_0^{x_1} (B - B_{01})\,\mathrm{d}x_1 \approx \mathrm{IFFT}_1 \frac{1}{\mathrm{i}k_{x_1}} \mathrm{FFT}_1 (B - B_{01}) \tag{80}$$

and

$$\int_0^{x_2} (B - B_{02})\,\mathrm{d}x_2 \approx \mathrm{IFFT}_2 \frac{1}{\mathrm{i}k_{x_2}} \mathrm{FFT}_2 (B - B_{02}), \tag{81}$$

where the components corresponding to $k_{x_1} = 0$ [in Eq. (80)] and $k_{x_2} = 0$ [in Eq. (81)] are set to zero.

The numerical approximation of the x_1 and η_1 derivatives in Eq. (58) are performed as

$$\frac{\partial}{\partial \eta_1} \left(-\mathrm{i}\eta_2 B_{01} + \frac{\partial}{\partial x_1} \right) G_1 \approx \mathrm{IFFT}_1 \left\{ \mathrm{D}_{\eta_1} \left[\mathrm{i}\left(k_{x_1} - \eta_2 B_{01}\right) \mathrm{FFT}_1 G_1 \right] \right\}, \tag{82}$$

where D_{η_1} is a difference approximation of the η_1 derivative. The form of the approximation (82) makes it possible to separate between incoming and outgoing waves at the boundary and to use numerically stable approximations of the η_1 derivative for the two cases: The factor $(k_{x_1} - \eta_2 B_{01})$ appearing in Eq. (82) is the same factor as in boundary condition (63); thus $(k_{x_1} - \eta_2 B_{01}) \geq 0$ describes outflow and $(k_{x_1} - \eta_2 B_{01}) < 0$ describes inflow at the boundary at $\eta_1 = \eta_{1,\max}$.

For negative η_1, function values are not represented on the numerical grid; even so, the boundary at $\eta_1 = 0$ is a symmetry boundary which can be "removed" by employing a symmetry relation similar to (29). In order to calculate the difference approximation D_{η_1} of the η_1 derivative used in Eq. (82), the symmetry is used to temporarily represent function values for negative η_1, so that the boundary at $\eta_1 = 0$ is removed, as follows.

Before performing the η_1 differentiation, the function values are temporarily moved, by symmetry, from the part of the domain with positive η_1 and negative η_2 to the part of the domain with negative η_1 and positive η_2, so that the η_1 domain goes from $\eta_1 = -\eta_{1,\max}$ to $\eta_1 = \eta_{1,\max}$ and the η_2 domain goes from $\eta_2 = 0$ to $\eta_2 = \eta_{2.\max}$. Thereafter the numerical η_1 differentiation is performed with appropriate boundary conditions, and finally the result is redistributed to the original domain with only nonnegative η_1.

In detail, these steps are performed as follows. The grid function to be differentiated numerically in Eq. (82) is

$$\left[\mathrm{i}\left(k_{x_1} - \eta_2 B_{01}\right) \mathrm{FFT}_1 G_1 \right] \equiv \tilde{g}_{i_1, i_2, j_1, j_2}, \tag{83}$$

where $i_1 = -(N_{x_1}/2 - 1), \ldots, N_{x_1}/2$ now represents Fourier components $(k_{x_1})_{i_1} = i_1 2\pi / L_1$ of $\tilde{g}$ since the Fourier transform FFT_1 has been applied in the x_1 direction. Because of the Fourier transforms in x_1, v_1, and v_2 space (yielding k_{x_1}, η_1, and η_2, respectively), the grid function $\tilde{g}$ obeys the symmetry property, similar to Eq. (29),

$$\tilde{g}_{i_1, i_2, -j_1, j_2} = \tilde{g}^*_{-i_1, i_2, j_1, -j_2}. \tag{84}$$

That is, in order to obtain the components of $\tilde{g}$ for negative j_1 (representing negative η_1), which are not represented on the numerical grid, the complex conjugates (superscript *) of these components are found on the numerical grid by the symmetry relation at the location

where i_1, j_1, and j_2 has opposite signs; therefore, in order to perform the η_1 derivative numerically, the components of $\tilde{g}$ are ordered in vectors as

$$\mathbf{g}_{i_1,i_2,j_2} = \begin{bmatrix} g_{-N_{\eta_1}} \\ g_{-N_{\eta_1}+1} \\ \vdots \\ g_{-1} \\ g_0 \\ g_1 \\ \vdots \\ g_{N_{\eta_1}} \end{bmatrix}_{i_1,i_2,j_2} \leftarrow \begin{bmatrix} \tilde{g}^*_{-i_1,i_2,N_{\eta_1},-j_2} \\ \tilde{g}^*_{-i_1,i_2,N_{\eta_1}-1,-j_2} \\ \vdots \\ \tilde{g}^*_{-i_1,i_2,1,-j_2} \\ \tilde{g}_{i_1,i_2,0,j_2} \\ \tilde{g}_{i_1,i_2,1,j_2} \\ \vdots \\ \tilde{g}_{i_1,i_2,N_{\eta_1},j_2} \end{bmatrix} \tag{85}$$

for each $j_2 = 0, 1, \ldots, N_{\eta_2}$, $i_1 = -(N_{x_1}/2 - 1), \ldots, N_{x_1}/2$, and $i_2 = 0, 1, \ldots, N_{x_2} - 1$, respectively.

The η_1 derivative $g' = \frac{\partial g}{\partial \eta_1} \approx \mathrm{D}_{\eta_1}\mathbf{g}_{i_1,i_2,j_2}$ is calculated using the standard fourth-order Padé scheme [10, 13]. For the inner points, the implicit approximation

$$g'_{j_1-1} + 4g'_{j_1} + g'_{j_1+1} = \frac{3}{\Delta\eta_1}\left(g_{j_1+1} - g_{j_1-1}\right), \tag{86}$$

where $j_1 = -N_{\eta_1} + 1, \ldots, -1, 0, 1, \ldots, N_{\eta_1} - 1$ is used.

The boundary at $\eta_1 = \eta_{1,\max}$ is an *outflow* boundary for $k_{x_1} \geq \eta_2 B_{01}$ [cf. Eq. (63)], where $k_{x_1} = 2\pi i_1/L_1$, i.e., for $i_1 \geq L_1\eta_{2,j_2}B_{01}/2\pi$. At the outflow boundary a one-sided approximation,

$$g'_{N_{\eta_1}} + 2g'_{N_{\eta_1}-1} = -\frac{1}{2\Delta\eta_1}\left(-5g_{N_{\eta_1}} + 4g_{N_{\eta_1}-1} + g_{N_{\eta_1}-2}\right), \tag{87}$$

is used, which gives a truncation error of order $\Delta\eta_1^3$ at the boundary. For $k_{x_1} < \eta_2 B_{01}$, the boundary at $\eta_1 = \eta_{1,\max}$ is an *inflow* boundary, at which a straight extrapolation,

$$g'_{N_{\eta_1}} = g'_{N_{\eta_1}-1}, \tag{88}$$

is used, which gives a truncation error of order $\Delta\eta_1^2$ at the boundary.

Correspondingly, the schemes at $\eta_1 = -\eta_{1,\max}$ become

$$g'_{-N_{\eta_1}} + 2g'_{-N_{\eta_1}+1} = \frac{1}{2\Delta\eta_1}\left(-5g_{-N\eta_1} + 4g_{-N\eta_1+1} + g_{-N\eta_1+2}\right) \tag{89}$$

and

$$g'_{-N\eta_1} = g'_{-N\eta_1+1} \tag{90}$$

for the *outflow* (where $k_{x_1} \leq \eta_2 B_{01}$) and *inflow* (where $k_{x_1} > \eta_2 B_{01}$) boundaries, respectively [cf. Eq. (66)].

The reason for using different approximations at the inflow and outflow boundaries is that the third-order approximation of the η_1 derivative used for the outflow of waves is not completely stable for the inflow of waves; a numerical test has shown that there are

some slowly growing modes which eventually destroy the numerical solution. This problem could be seen in some numerical solutions of the simple two-dimensional problem (48), with $k_{x_1} = k_{x_2} = 0$, with random numbers as the initial condition.

The second-order approximations (88) and (90), giving a formal overall accuracy of at most three, can be justified as follows: This boundary condition only affects waves which reach the boundary, and which then turn back into the domain again. Parts of these waves are lost through the outflow boundary. The loss of information through the outflow boundary is of zeroth order, i.e., it is independent of $\Delta\eta_1$ and $\Delta\eta_2$, while the local truncation error for the inflow boundary is of second order in $\Delta\eta_1$ and $\Delta\eta_2$. This means that even if the inflow boundary is resolved with higher accuracy, the gain in numerical accuracy does not contribute much to solving the physical problem more accurately, because of the information lost through the outflow boundary. If these waves are important for the physical problem, then the boundary must instead be moved further away from the origin. The only important property of the inflow boundary is to be robust, not creating waves and noise.

Equations (86)–(90) form a tridiagonal equation system for each component i_1, i_2, j_2 in Eq. (85), with each system having $2N_{\eta_1} + 1$ complex-valued unknowns. When the solution vector $\mathbf{g}'$ has been calculated, the numerical differentiation of $\tilde{g}$ is obtained as

$$\begin{bmatrix} \tilde{g}'_{-i_1,i_2,N_{\eta_1},-j_2} \\ \tilde{g}'_{-i_1,i_2,N_{\eta_1}-1,-j_2} \\ \vdots \\ \tilde{g}'_{-i_1,i_2,1,-j_2} \\ \tilde{g}'_{i_1,i_2,0,j_2} \\ \tilde{g}'_{i_1,i_2,1,j_2} \\ \vdots \\ \tilde{g}'_{i_1,i_2,N_{\eta_1},j_2} \end{bmatrix} \leftarrow \begin{bmatrix} -(g')^*_{-N_{\eta_1}} \\ -(g')^*_{-N_{\eta_1}+1} \\ \vdots \\ -(g')^*_{-1} \\ g'_0 \\ g'_1 \\ \vdots \\ g'_{N_{\eta_1}} \end{bmatrix}_{i_1,i_2,j_2} ; \tag{91}$$

i.e., it is used that for the η_1 derivative of $\tilde{g}$, the real part is an odd function with respect to (i_1, j_1, j_2), and the imaginary part is an even function with respect to the same vector [see a similar discussion after Eq. (29)]. Finally, the numerical inverse Fourier transform in x_1 space yields the approximation (82).

The boundary operator in Eq. (63) is calculated by using the approximation (80) for the numerical integration of $(B - B_{01})$, and by using the approximation FFT_1 and IFFT_1 for F_1 and F_1^{-1}, respectively.

The algorithm above for calculating the x_1 and η_1 derivatives will, with small modifications, hold also for the differentiation in x_2 and η_2 space. A difference is that function values are already represented on the numerical grid for negative η_2, and it is therefore not necessary to artificially extend function values to negative η_2 by symmetry by ordering of vectors similar to that in Eqs. (85), (91) Making approximations similar to Eq. (82) (but in x_2 and η_2 space instead of x_1 and η_1 space), the η_2 differentiation can therefore be performed directly on the function

$$\left[\mathrm{i}\left(k_{x_2} + \eta_1 B_{02}\right)\mathrm{FFT}_2 G_2\right] \equiv \tilde{g}_{i_1,i_2,j_1,j_2}, \tag{92}$$

with $j_1 = 0, 1, \ldots, N_{\eta_1}$, $j_2 = -N_{\eta_2}, 1, \ldots, N_{\eta_2}$, $i_1 = 0, \ldots, N_{x_1}$, and $i_2 = -(N_{x_2}/2 - 1)$,

$1, \ldots, N_{x_2} - 1$, and taking into account the boundary conditions (64) and (65). We omit the detailed discussion about the x_2 and η_2 differentiations here.

In order to reduce aliasing effects in the x_1 and x_2 directions for nonlinear problems, a sixth-order dissipative term,

$$\delta \Delta x_1^4 \left(\frac{\partial^6 \hat{f}}{\partial x_1^6} + \frac{\partial^6 \hat{f}}{\partial x_2^6} \right), \tag{93}$$

is added to the right-hand side of Eq. (58), where the constant δ is set to some small positive number. The derivatives are approximated by centred second-order approximations.

3.3. *Stability Constraints on the Time Step*

When solving a dependent linear system of differential equations in time, an explicit time-stepping scheme has a Courant condition [20]

$$\Delta t < \frac{\rho}{\lambda_{\max}}, \tag{94}$$

which must be fulfilled for stability. The constant ρ depends on the scheme and $\lambda_{\max}$ is typically the maximum modulus of the eigenvalues of the semidisecretised system. For the system studied in the present article, the eigenvalues are close to imaginary. The stability region for the Runge–Kutta scheme along the imaginary axis goes from $-i\sqrt{8}$ to $i\sqrt{8}$, which gives

$$\rho = \sqrt{8}. \tag{95}$$

In the equation to be solved,

$$\frac{\partial \hat{f}}{\partial t} - i \frac{\partial^2 \hat{f}}{\partial x_1 \partial \eta_1} - i \frac{\partial^2 \hat{f}}{\partial x_2 \partial \eta_2} + i(E_1 \eta_1 + E_2 \eta_2) \hat{f} + B \eta_1 \frac{\partial \hat{f}}{\partial \eta_2} - B \eta_2 \frac{\partial \hat{f}}{\partial \eta_1} = 0, \tag{96}$$

the coefficients $(E_1 \eta_1 + E_2 \eta_2)$, $B\eta_1$, and $B\eta_2$ depend on all the variables $(x_1, x_2, \eta_1, \eta_2, t)$, which complicates an exact stability analysis. The analysis can be simplified considerably by replacing the coefficients with their maximum absolute values at each time, and by assuming the time dependence to be weak for the resulting coefficients. By this procedure, Eq. (96) is changed into

$$\begin{aligned} &\frac{\partial \hat{f}}{\partial t} - i \frac{\partial^2 \hat{f}}{\partial x_1 \partial \eta_1} - i \frac{\partial^2 \hat{f}}{\partial x_2 \partial \eta_2} + i(E_{1,\max} \eta_{1,\max} + E_{2,\max} \eta_{2,\max}) \hat{f} \\ &\quad + B_{\max} \eta_{1,\max} \frac{\partial \hat{f}}{\partial \eta_2} - B_{\max} \eta_{2,\max} \frac{\partial \hat{f}}{\partial \eta_1} = 0, \end{aligned} \tag{97}$$

where $E_{1,\max}(t)$, $E_{2,\max}(t)$, and $B_{\max}(t)$ are the maximum absolute values (max norm) of E_1, E_2, and B at each time. By neglecting the time dependence of these absolute values, a von Neumann stability analysis can be carried through. The resulting maximum eigenvalue is

$$\begin{aligned} \lambda_{\max} = {} & K_{x_1} K_{\eta_1} + K_{x_2} K_{\eta_2} + E_{1,\max} \eta_{1,\max} + E_{2,\max} \eta_{2,\max} \\ & + B_{\max} \eta_{1,\max} K_{\eta_2} + B_{\max} \eta_{2,\max} K_{\eta_1}, \end{aligned} \tag{98}$$

where K_{x_1}, K_{x_2}, K_{η_1}, and K_{η_2} are the maximum values of the approximations of wavenumbers produced by the numerical approximations of the x_1, x_2, η_1, and η_2 derivatives, respectively, given by

$$K_{x_1} = \frac{\pi}{\Delta x_1}, \quad K_{x_2} = \frac{\pi}{\Delta x_2}, \quad K_{\eta_1} = \frac{\sqrt{3}}{\Delta \eta_1}, \quad K_{\eta_2} = \frac{\sqrt{3}}{\Delta \eta_2}, \tag{99}$$

where K_{x_1} and K_{x_2} are produced by the pseudospectral method and K_{η_1} and K_{η_2} are produced by the Padé scheme. The resulting maximum eigenvalue is

$$\begin{aligned}\lambda_{\max} = {} & \frac{\pi}{\Delta x_1}\frac{\sqrt{3}}{\Delta \eta_1} + \frac{\pi}{\Delta x_2}\frac{\sqrt{3}}{\Delta \eta_2} + E_{1,\max}\eta_{1,\max} + E_{2,\max}\eta_{2,\max} \\ & + B_{\max}\eta_{1,\max}\frac{\sqrt{3}}{\Delta \eta_2} + B_{\max}\eta_{2,\max}\frac{\sqrt{3}}{\Delta \eta_1}.\end{aligned} \tag{100}$$

Introducing a generalised CFL number [20], condition (94) can be expressed as

$$\Delta t = \mathrm{CFL}\frac{\rho}{\lambda_{\max}}, \tag{101}$$

where the positive CFL number obeys the condition

$$\mathrm{CFL} < 1 \tag{102}$$

for stability. For the numerical experiments in the present article, the CFL number CFL $=$ 0.9 has been used. As $\lambda_{\max}$ varies with time, the time step Δt is adapted to maintain numerical stability.

The artificial boundaries at $\eta_1 = \eta_{1,\max}$ and at $\eta_2 = \pm\eta_{2,\max}$ has not been included in the present analysis. For these boundaries, we rely on the analysis of model problems performed by Lele [13] and by Gustafsson and Olsson [10] for the outflow boundaries, and on long-time numerical experiments (see Section 4).

3.4. *The Choice of Domain and Grid Sizes*

The present section briefly discusses the choices of the numerical domain and grid sizes to be made in $\boldsymbol{\eta}$ space. We restrict the discussion to one dimension, $\eta_1 = \eta$, only.

Consider the following two problems when representing a function $f(v)$ on an equidistant grid.

1. The function is defined for all velocities, but numerically one has to truncate the solution domain at some high velocity $v_{\max}$, where the function values have become small enough.

2. The function may contain fine structures in the v direction, and one has to use a fine enough grid to represent these fine structures.

These two problems have their duals in the inverse Fourier transformed variables; a function which is less localised around $v = 0$ leads to a more oscillatory function in the η space, and a more oscillatory function in v space leads to a less localised function in η space. To be

precise, the two problems are converted to the following:

1. Assuming that the maximum velocity for particles is $v = v_{\max}$, then after Fourier transforming the function $f(v)$, the quantity $k_{\eta,\max} = v_{\max}$ will be the maximum "wavenumber" in η direction, and the minimum "wavelength" will then be $\lambda_{\eta,\min} = 2\pi/k_{\eta,\max} = 2\pi/v_{\max}$. According to the Nyqvist sampling theorem one needs at least two grid points per wavelength to represent the solution, so the condition on the grid size becomes $\Delta\eta < \lambda_{\eta,\min}/2 = \pi/v_{\max}$.

2. Assuming that the shortest "wavelength" to be resolved in the v direction is $\lambda_{v,\min}$, the highest wavenumber in the v direction becomes $k_{v,\max} = 2\pi/\lambda_{v,\min}$. After Fourier transformation, this gives a condition on the domain size in the η direction as $\eta_{\max} \geq k_{v,\max} = 2\pi/\lambda_{v,\min}$.

Thus, the value of the grid size $\Delta\eta$ must be smaller than $\pi/v_{\max}$ and the size of the domain must be larger than $-2\pi/\lambda_{v,\min} \leq \eta \leq 2\pi/\lambda_{v,\min}$ in order to represent the solution on the grid.

In most real problems, however, the exact values of the largest particle velocities $v_{\max}$ and the necessary resolution $\lambda_{v,\min}$ are not known beforehand, and it is necessary to oversample the problem in order to achieve numerical accuracy; the discretisation and numerical approximation of the η derivative lead to a periodicity v space, where the effective particle velocities follow from the dispersive properties of the numerical differentiation in η space. If the grid in η space is too coarse, particles with high positive or negative velocities will have effective velocities deviating significantly from the real velocity: For example, assuming a cold particle stream at velocity v_0 with the distribution function $f(v) = \delta(v - v_0)$, where δ is the Dirac delta measure, yields in the Fourier transformed space the function $\hat{f}(\eta) = \exp(i\eta v_0)$. Differentiating this function exactly with respect to η yields the velocity v_0 as a factor in front of $\hat{f}$, but using the numerical Padé approximation [cf. Eq. (86)] to calculate the derivative yields the effective velocity

$$v_{\text{eff}} = v_0 \frac{3}{v_0 \Delta\eta} \frac{\sin(v_0 \Delta\eta)}{[2 + \cos(v_0 \Delta\eta)]}, \tag{103}$$

which approaches v_0 as $\Delta\eta \to 0$. It is apparent that the deviation of the effective velocity v_{eff} from real velocity v_0 may be significant if the $\Delta\eta$ chosen is too large.

Therefore, the inequality $\Delta\eta < \pi/v_{\max}$ should be fulfilled with a sufficiently large margin for correctly representing particle velocities. The inequality $\eta_{\max} \geq 2\pi/\lambda_{v,\min}$ chosen should be sufficiently large to resolve the desired filamentation in velocity space.

The number of grid points needed to represent the function $f(x, \eta, t)$ on the interval $0 \leq \eta \leq \eta_{\max}$ [for negative η, the symmetry relation (29) is used] is

$$N_\eta = \frac{\eta_{\max}}{\Delta\eta} > 2\frac{v_{\max}}{\lambda_{v,\min}}. \tag{104}$$

For the original function $f(v)$, one would have to represent the function on the domain $-v_{\max} \leq v \leq v_{\max}$, with the grid size $\Delta v < \lambda_{v,\min}/2$ according to the sampling theorem. This gives the number of grid points in the v direction as

$$N_v = \frac{2v_{\max}}{\Delta v} > 4\frac{v_{\max}}{\lambda_{v,\min}}. \tag{105}$$

Thus one needs twice as many grid points to represent the original function $f(v)$ on a grid, compared to representing the Fourier transformed function $\hat{f}(\eta)$ on a grid. However, the function $\hat{f}(\eta)$ is complex valued so the *amount of data* needed is the same for $\hat{f}(\eta)$ as for $\hat{f}(v)$.

4. NUMERICAL RESULTS

4.1. *Stability Tests*

In order to assess the stability of the numerical scheme, numerical tests were carried out with random numbers as initial conditions, and the relative change of the energy norm of the solution was calculated as a function of time.

The simulation domain was chosen to be $0 \le x_1 \le 4\pi$, $0 \le x_2 \le 4\pi$, $0 \le \eta_1 \le 10$, and $-10 \le \eta_2 \le 10$ with the corresponding number of intervals $N_{x_1} = N_{x_2} = 10$, $N_{\eta_1} = 40$, and $2N_{\eta_2} = 80$. The initial condition on the complex function values was random numbers, chosen uniformly in the interval between -0.5 and $+0.5 \times 10^{-5}$. The number of time steps were chosen to be $N_t = 100\,000$, with the time step Δt chosen adaptively according to Section 3.3 with CFL $= 0.9$. No numerical dissipation was used.

Two simulations were carried out: In the first run, the magnetic field was chosen to be constant, $B = 1/\sqrt{10}$ (see curve a in Fig. 1), and in the second run, the magnetic field was chosen to be x_1 and x_2 dependent, $B = \sin[0.5(x_1 + x_2)]/\sqrt{10}$ (see curve b in Fig. 1). These two simulations are motivated by the fact that the boundary conditions at $\eta_1 = \eta_{1,\max}$ and $\eta_2 = \eta_{2,\max}$ are dependent on B [see Eqs. (63)–(65)]. All quantities has been written out in dimensional units in Fig. 1.

The relative norms of the solution decreased from unity to close to zero; thus no instabilities could be seen in the two simulations. The large number of time steps ensured that any growing modes should be visible in the simulations; that was not the case and we therefore conclude that the scheme is robust and damps out noise over long time intervals.

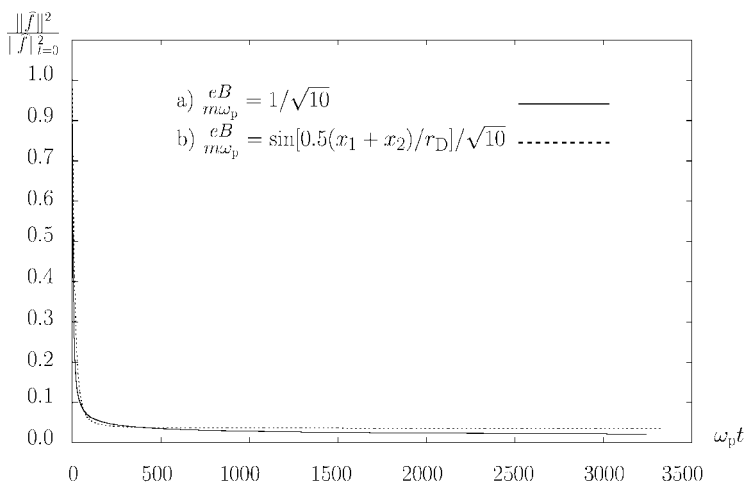

FIG. 1. Two long-term stability tests with random numbers as initial conditions. The curves show the relative change of the energy norm as a function of time: (a) constant magnetic field; (b) **x**-dependent magnetic field. Both curves have the value unity at time zero.

4.2. *The Conservation of Particles*

It is easy to show that the numerical scheme conserves the total number of particles (35) exactly, approximated by the formula

$$N = (2\pi)^2 \sum_{i_1=0}^{N_{x_1}-1} \sum_{i_2=0}^{N_{x_2}-1} \hat{f}_{i_1,i_2,0,0} \Delta x. \tag{106}$$

The sum only picks up the zeroth Fourier component of $\hat{f}_{i_1,i_2,0,0}$, corresponding to $k_{x_1} = k_{x_2} = 0$, and that component is left unchanged since the terms, containing the x_1 and x_2 derivatives in Eq. (58) with the approximations (76) and (77), vanish. Along the boundary $\eta_1 = \eta_2 = 0$ the rest of the terms, which are multiplied with η_1 or η_2, also vanish. This result has been verified in all numerical experiments presented in this article, where the number of particles has been conserved by the numerical scheme up to the precision of the computer.

4.3. *Upper Hybrid Waves and Electron Bernstein Waves*

In order to verify that the numerical scheme reproduces waves with correct dispersive properties, a numerical test which simulates electrostatic upper hybrid waves and electron Bernstein waves was carried out.

The spatial dependence of the distribution function was here restricted to one dimension, x_1, while the function was assumed to be uniform in the x_2 dimension. The simulation domain was chosen to be $0 \le x_1 \le 40\pi$, $0 \le \eta_1 \le 10$, and $0 \le \eta_2 \le 10$ with the corresponding number of intervals $N_{x_1} = 120$, $N_{\eta_1} = 40$, and $2N_{\eta_2} = 80$. The initial condition was chosen to be a sum of electrostatic waves with all possible wavenumbers in the original $(\mathbf{x}, \mathbf{v}, t)$ variables chosen as

$$f(x_1, x_2, v_1, v_2, 0) = \left[1 + A \sum_{i_1=1}^{59} i_1 \sin(0.05 i_1 x_1)\right] f_0(v_1, v_2), \tag{107}$$

$$f_0(v_1, v_2) = \frac{1}{2\pi} \exp\left[-\frac{1}{2}\left(v_1^2 + v_2^2\right)\right], \tag{108}$$

which gives the initial condition in the Fourier transformed variables used in the simulation as

$$\hat{f}(x_1, x_2, \eta_1, \eta_2, 0) = \left[1 + A \sum_{i_1=1}^{59} i_1 \sin(0.05 i_1 x_1)\right] \hat{f}_0(\eta_1, \eta_2), \tag{109}$$

$$\hat{f}_0(\eta_1, \eta_2) = \frac{1}{(2\pi)^2} \exp\left[-\frac{1}{2}\left(\eta_1^2 + \eta_2^2\right)\right], \tag{110}$$

with the amplitude set to $A = 0.0001$; the small amplitude A was chosen so that the problem would be close to linear. The magnetic field was kept constant in the simulation, $B = 1/\sqrt{10}$, giving the ratio $\omega_p^2/\omega_c^2 = 10$ between the plasma frequency ω_p and the electron gyro frequency $\omega_c = eB/m$, in dimensional units. The time step Δt was chosen adaptively according to Section 3.3 with CFL $= 0.9$, and the number of time steps was $N_t = 23\,500$; the end time was $T_{\text{end}} = 921\omega_p^{-1}$. No numerical dissipation was used.

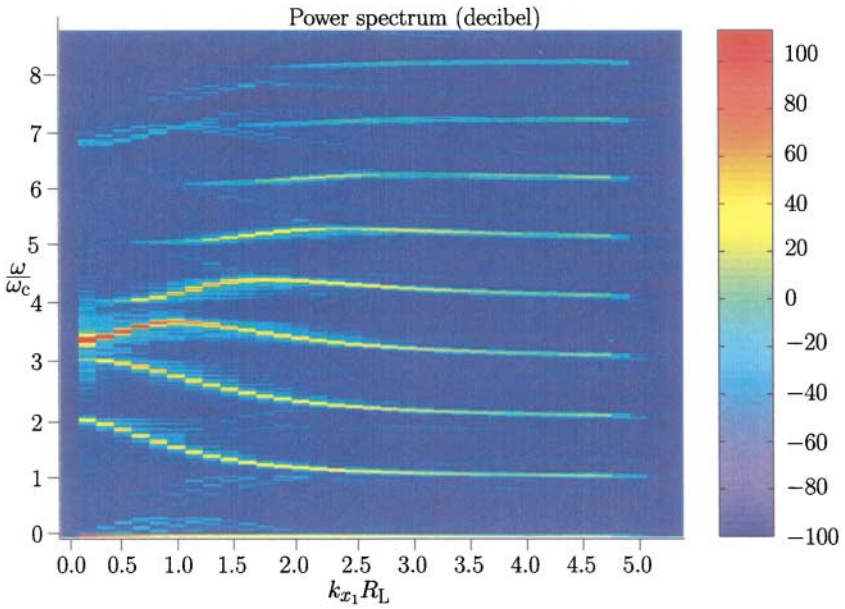

FIG. 2. Power spectrum in (ω, k_{x_1}) space for electrostatic upper hybrid waves and electron Bernstein waves. The electric energy is concentrated at the dispersion curves for the linear eigenmodes.

In order to analyse the result, the electric field component E_1 was Fourier transformed in the x_1 space and time (using a Hamming window). The resulting power spectrum is shown in Fig. 2, in a logarithmic scale. All quantities are given in dimensional units. The wavenumber k_{x_1} has been multiplied by $R_L = v_{th}/\omega_c = \sqrt{k_B T/m}/\omega_c$, and the frequency ω has been divided by the electron gyro frequency $\omega_c = eB/m$, in order to make the comparison with theoretical results easier.

Linear eigenmodes of the system have been calculated theoretically by Crawford and Tataronis [5], who made plots of the dispersion curves for a few values of the magnetic field; one of the cases is $\omega_p^2/\omega_c^2 = 10$, giving the same value for the magnetic field as in the setup for the present simulation. The corresponding dispersion curves are also cited in a book by Chen [2]. (There appears to be an error in the scaling in the diagram depicted in [2]: Chen uses the scaling $r_L = v_{th}/\omega_c$ of the wavenumbers (see Fig. 7-34 in [2]) while Crawford and Tataronis use the corresponding scaling $R = v_{th}/\sqrt{2}\omega_c$ (see Fig. 1 and Eq. (9) in [5]). Both authors use the definition $v_{th} = \sqrt{2k_B T/m}$ of the thermal velocity.)

In the simulation, the electric energy was concentrated along the linear Bernstein eigenmodes (see Fig. 2), in a very good agreement with the linear theory [2, 5]. Even though in the simulation low values were chosen for the amplitude of the initial condition, a nonlinear effect can be seen in the power spectrum: A second harmonic of the upper hybrid wave can be seen slightly below $\omega/\omega_c = 7$ for small values of k_{x_1}, where the first harmonic of the upper hybrid oscillation is slightly above $\omega/\omega_c = 3$.

The damping of waves for $k_{x_2} R_L > 5$ is a numerical effect; if the boundaries $\eta_{1,\max}$ and $\eta_{2,\max}$ are given larger values, then these waves become undamped, in agreement with theory (see Section 3.4 for a discussion about the choice of domain size).

4.4. *Landau Damping and Reduction of the Recurrence Phenomenon*

In order to verify that waves are absorbed by the boundaries $\eta_1 = \eta_{1,\max}$ and $\eta_2 = \eta_{2,\max}$, and that thereby the recurrence phenomenon is reduced, numerical experiments with unmagnetised plasma, $B = 0$, were carried out: The initial condition in the original variables was chosen to be

$$f(x_1, x_2, v_1, v_2, 0) = \left[1 + A\cos\left(k_{x_1}x_1 + k_{x_2}x_2\right)\right] f_0(v_1, v_2), \tag{111}$$

$$f_0(v_1, v_2) = \frac{1}{2\pi}\exp\left[-\frac{1}{2}\left(v_1^2 + v_2^2\right)\right], \tag{112}$$

which gives the initial condition in the Fourier transformed variables used in the simulation as

$$\hat{f}(x_1, x_2, \eta_1, \eta_2, 0) = \left[1 + A\cos\left(k_{x_1}x_1 + k_{x_2}x_2\right)\right] \hat{f}_0(\eta_1, \eta_2), \tag{113}$$

$$\hat{f}_0(\eta_1, \eta_2) = \frac{1}{(2\pi)^2}\exp\left[-\frac{1}{2}\left(\eta_1^2 + \eta_2^2\right)\right], \tag{114}$$

with the amplitude set to $A = 0.0002$, making the waves close to linear. The wavenumbers k_{x_1} and k_{x_2} were chosen so that $k^2 = k_{x_1}^2 + k_{x_2}^2 = 0.5^2$; this choice of k makes the electrostatic Langmuir waves strongly Landau damped. Using the algorithm in the WHAMP [19] program for calculating the frequency according to the linear dispersion law, we obtained numerical values on the real and imaginary parts of the frequency for the wavenumber $k = 0.5r_D^{-1}$ as $\omega^{Re} = 1.4156\omega_p$ and $\omega^{1m} = -0.15337\omega_p$, respectively.

The first numerical experiment was restricted to one spatial dimension, x_1; the wavenumbers were chosen to be $k_{x_1} = 0.5$ and $k_{x_2} = 0$, and the domain in x_1 was chosen large enough to contain one wavelength, $0 < x_1 < 4\pi$, with the number of grid points $N_{x_1} = 10$. In the η_1 and η_2 space, the simulation domain was chosen to be $0 \le \eta_1 \le 20$ and $-20 \le \eta_2 \le 20$, with the number of grid points $N_{\eta_1} = 150$ and $2N_{\eta_2} = 300$. The number of time steps taken were 2554 in the simulation, ending at time $t_{end} = 200$.

The numerical results can be seen in Fig. 3 (top); the modulus of the $\hat{x}_1$ component of the electric field has been plotted as a function of time. All quantities in the figure have been written out in dimensional units. Curve a in Fig. 3 shows the electric field for the case where all function values have been set to zero at the boundary $\eta_1 = \eta_{1,\max}$, and Fig. 3, curve b, shows the electric field for the case where the outflow boundary conditions (63)–(65) have been used at $\eta_1 = \eta_{1,\max}$ and $\eta_2 = \pm\eta_{2,\max}$.

The second numerical experiment was performed with two spatial dimensions, with an obliquely propagating wave; the wavenumbers were chosen to be $k_{x_1} = k_{x_2} = 0.5/\sqrt{2}$, and the domain in x_1 and x_2 space was chosen to be large enough to contain one wavelength, $0 < x_1 < 4\sqrt{2}\pi$ and $0 < x_2 < 4\sqrt{2}\pi$, with the number of grid points $N_{x_1} = N_{x_2} = 10$. In the η_1 and η_2 space, the simulation domain was chosen to be $0 \le \eta_1 \le 20$ and $-20 \le \eta_2 \le 20$, with the number of grid points $N_{\eta_1} = 150$ and $2N_{\eta_2} = 300$. The number of time steps taken were 3610 in the simulation, ending at time $t_{end} = 200$.

The numerical results for this experiment are shown in the bottom of Fig. 3; the modulus of the $\hat{x}_1$ component of the electric field has been plotted as a function of time. Curve c in Fig. 3 shows the electric field for the case where all function values have been set to zero at the boundaries $\eta_1 = \eta_{1,\max}$ and $\eta_2 = \eta_{2,\max}$, and Fig. 3, curve d, shows the electric field for

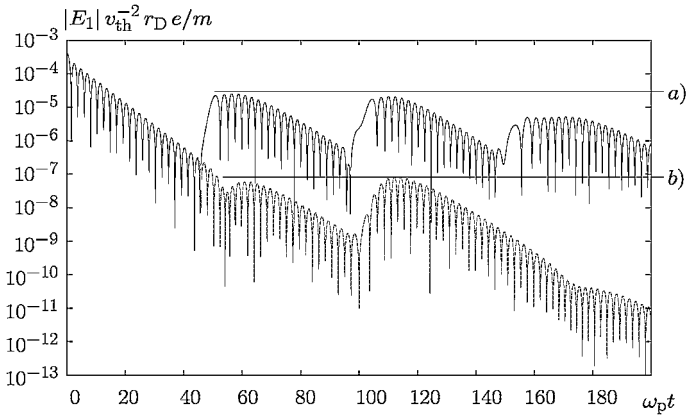

(a) $k_{x_1} = 0.5\, r_{\rm D}^{-1}$, $k_{x_2} = 0\, r_{\rm D}^{-1}$. Curve a): $\widehat{f} = 0$ at $\eta_1 = \eta_{1,\max}$ and $\eta_2 = \pm\eta_{2,\max}$, b): outflow boundary at $\eta_1 = \eta_{1,\max}$ and $\eta_2 = \pm\eta_{2,\max}$.

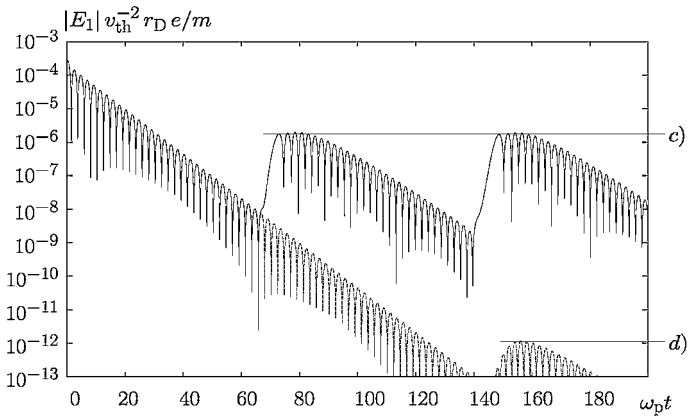

(b) $k_{x_1} = k_{x_2} = (0.5/\sqrt{2})\, r_{\rm D}^{-1}$. Curve c): $\widehat{f} = 0$ at $\eta_1 = \eta_{1,\max}$ and $\eta_2 = \pm\eta_{2,\max}$, d): outflow boundaries at $\eta_1 = \eta_{1,\max}$ and $\eta_2 = \pm\eta_{2,\max}$.

FIG. 3. The modulus of the electric field as a function of time. (Curves a–d). The impact of the recurrence phenomenon on the electric field.

the case where the outflow boundary conditions (63) and (64) have been used at $\eta_1 = \eta_{1,\max}$ and $\eta_2 = \pm\eta_{2,\max}$.

As is clear from Fig. 3, the solutions are initially exponentially damped. By measuring the slope of the curves and by measuring the time for a number of periods before the recurrence phenomenon takes place, we found the damping to be $\omega^{\rm Im} \approx -0.153$ and the real frequency to be $\omega^{\rm Re} \approx -1.41$ in both numerical experiments, in good agreement with the result achieved by the WHAMP algorithms.

At about $t = 50\omega_{\rm p}^{-1}$ (Fig. 3, top) and about $t = 70\omega_{\rm p}^{-1}$ (Fig. 3, bottom), one can see the recurrence phenomenon resulting in sudden artificial increases in the electric field. In the top of Fig. 3, one can see that the recurrence phenomenon causes the electric field to rise to about $1/10$ of the initial amplitude (curve a) for the case where the η_1 boundaries has been set to zero, and to rise to less than $1/1000$ of the initial amplitude (curve b) for the case with the outflow condition at the η_1 boundary. Correspondingly, in the bottom of Fig. 3, one can

see that the recurrence phenomenon causes the electric field to rise to somewhat less than $1/100$ of the initial amplitude (curve c) for the case where the η_1 and η_2 boundaries has been set to zero, and to rise to less than 10^{-8} of the initial amplitude (curve d) for the case with the outflow conditions at the η_1 and η_2 boundaries.

It is apparent from this numerical investigation that the outgoing wave boundary conditions prevent, to a large extent, waves from returning back and ruining the calculations by the recurrence phenomenon, while the simple Dirichlet-type boundary conditions lead to a stronger recurrence phenomenon, which may destroy the numerical results. The method of setting the boundary values to zero was advised for the Fourier–Fourier method [1], which is a method similar to (but not identical to) the method described in the present article.

We found the numerical values of the frequency and Landau damping to be in good agreement with linear theory for the unmagnetised case.

5. CONCLUSIONS

The boundary conditions for the two-dimensional Fourier transformed Vlasov–Poisson system has been studied, and a well-posed outflow boundary condition in the Fourier transformed velocity space has been derived.

The system has been solved numerically, using high-order numerical approximations. It was shown numerically that the recurrence phenomenon was reduced, and that the numerical scheme was stable. The simulations reproduced known theoretical physical results to a high degree.

6. DISTRIBUTION OF THE COMPUTER CODE

The Fortran 90 code which has been used to produce the numerical results in the present article can be found on the internet Web site http://www.physics.irfu.se/∼be.

APPENDIX: PROOF OF THE WELL-POSEDNESS OF THE PROBLEM

In the Appendix, a proof is given of the well-posedness of the Fourier transformed Vlasov equation (58) [equivalent to Eq. (22)], restricted to a bounded domain and with the boundary conditions given in Section 2.6.

We will use the short notation for the integral expressions,

$$\int\int_{\mathbf{x}} \mathrm{d}^2x \equiv \int_{x_1=0}^{L_1}\int_{x_2=0}^{L_2} \mathrm{d}x_2\,\mathrm{d}x_1 \quad \text{and} \quad \int\int_{\eta} \mathrm{d}^2\eta \equiv \int_{\eta_1=0}^{\eta_{1,\max}}\int_{\eta_2=-\eta_{2.\max}}^{\eta_{2,\max}} \mathrm{d}\eta_2\,\mathrm{d}\eta_1, \quad (115)$$

when convenient in the proof.

The problem is well-posed if the squared energy norm of the solution

$$\|\hat{f}\|^2 = \int\int_{\mathbf{x}}\int\int_{\eta} |\hat{f}|^2\,\mathrm{d}^2\eta\,\mathrm{d}^2x = \int\int_{\mathbf{x}}\int\int_{\eta} \hat{f}\,\hat{f}^*\,\mathrm{d}^2\eta\,\mathrm{d}^2x \quad (116)$$

is bounded for all times [20]. (The superscript * denotes complex conjugation.) In the following, we prove that the squared norm (116) is nonincreasing with time. Taking the

time derivative of the squared norm,

$$\frac{\mathrm{d}\|\hat{f}\|^2}{\mathrm{d}t} = \int\int_{\mathbf{x}}\int\int_{\eta}\left(\hat{f}^*\frac{\partial\hat{f}}{\partial t} + \hat{f}\frac{\partial\hat{f}^*}{\partial t}\right)\mathrm{d}^2\eta\ \mathrm{d}^2x, \tag{117}$$

and then replacing the time derivatives with the help of Eq. (58) gives

$$\begin{aligned}\frac{\mathrm{d}\|\hat{f}\|^2}{\mathrm{d}t} = \int\int_{\mathbf{x}}\int\int_{\eta}\Bigg(&\hat{f}^*\Bigg\{\mathrm{i}\exp\left[\mathrm{i}\eta_2\int_0^{x_1}(B-B_{01})\,\mathrm{d}x_1\right]\frac{\partial}{\partial\eta_1}\left(-\mathrm{i}\eta_2 B_{01}+\frac{\partial}{\partial x_1}\right)G_1\\ &+\mathrm{i}\exp\left[-\mathrm{i}\eta_1\int_0^{x_2}(B-B_{02})\,\mathrm{d}x_2\right]\frac{\partial}{\partial\eta_2}\left(\mathrm{i}\eta_1 B_{02}+\frac{\partial}{\partial x_2}\right)G_2+\mathrm{i}(\eta_1E_1+\eta_2E_2)\hat{f}\Bigg\}\\ &+\hat{f}\Bigg\{-\mathrm{i}\exp\left[-\mathrm{i}\eta_2\int_0^{x_1}(B-B_{01})\,\mathrm{d}x_1\right]\frac{\partial}{\partial\eta_1}\left(\mathrm{i}\eta_2 B_{01}+\frac{\partial}{\partial x_1}\right)G_1^*\\ &-\mathrm{i}\exp\left[\mathrm{i}\eta_1\int_0^{x_2}(B-B_{02})\,\mathrm{d}x_2\right]\frac{\partial}{\partial\eta_2}\left(-\mathrm{i}\eta_1 B_{02}+\frac{\partial}{\partial x_2}\right)G_2^*\\ &-\mathrm{i}(\eta_1E_1+\eta_2E_2)\hat{f}^*\Bigg\}\Bigg)\mathrm{d}^2\eta\ \mathrm{d}^2x,\end{aligned} \tag{118}$$

where all terms containing E_1 and E_2 cancel out. In terms of the functions G_1 and G_2, introduced in Eqs. (59), (60), the above equation can be rewritten

$$\begin{aligned}\frac{\mathrm{d}\|\hat{f}\|^2}{\mathrm{d}t} &= \int\int_{\mathbf{x}}\int\int_{\eta}\left[\mathrm{i}G_1^*\frac{\partial}{\partial\eta_1}\left(-\mathrm{i}\eta_2 B_{01}+\frac{\partial}{\partial x_1}\right)G_1+\mathrm{i}G_2^*\frac{\partial}{\partial\eta_2}\left(\mathrm{i}\eta_1 B_{02}+\frac{\partial}{\partial x_2}\right)G_2\right.\\ &\quad\left.-\mathrm{i}G_1\frac{\partial}{\partial\eta_1}\left(\mathrm{i}\eta_2 B_{01}+\frac{\partial}{\partial x_1}\right)G_1^*-\mathrm{i}G_2\frac{\partial}{\partial\eta_2}\left(-\mathrm{i}\eta_1 B_{02}+\frac{\partial}{\partial x_2}\right)G_2^*\right]\mathrm{d}^2\eta\ \mathrm{d}^2x\\ &= \int\int_{\mathbf{x}}\int\int_{\eta}\left[\mathrm{i}\frac{\partial}{\partial\eta_1}\left(G_1^*\frac{\partial G_1}{\partial x_1}\right)-\mathrm{i}\frac{\partial}{\partial x_1}\left(G_1\frac{\partial G_1^*}{\partial\eta_1}\right)+\mathrm{i}\frac{\partial}{\partial\eta_2}\left(G_2^*\frac{\partial G_2}{\partial x_2}\right)\right.\\ &\quad\left.-\mathrm{i}\frac{\partial}{\partial x_2}\left(G_2\frac{\partial G_2^*}{\partial\eta_2}\right)+\eta_2 B_{01}\frac{\partial}{\partial\eta_1}(G_1G_1^*)-\eta_1 B_{02}\frac{\partial}{\partial\eta_2}(G_2G_2^*)\right]\mathrm{d}^2\eta\ \mathrm{d}^2x,\end{aligned} \tag{119}$$

which can be integrated one step,

$$\begin{aligned}\frac{\mathrm{d}\|\hat{f}\|^2}{\mathrm{d}t} &= \int\int_{\mathbf{x}}\int_{\eta_2=-\eta_{2,\max}}^{\eta_{2,\max}}\left[\mathrm{i}G_1^*\frac{\partial G_1}{\partial x_1}+\eta_2 B_{01}G_1^*G_1\right]_{\eta_1=0}^{\eta_{1,\max}}\mathrm{d}\eta_2\,\mathrm{d}^2x\\ &\quad+\int\int_{\mathbf{x}}\int_{\eta_1=0}^{\eta_{1,\max}}\left[\mathrm{i}G_2^*\frac{\partial G_2}{\partial x_2}-\eta_1 B_{02}G_2^*G_2\right]_{\eta_2=-\eta_{2,\max}}^{\eta_{2,\max}}\mathrm{d}\eta_1\,\mathrm{d}^2x\\ &\quad+\int_{x_2=0}^{L_2}\int\int_{\eta}\left[-G_1\frac{\partial G_1^*}{\partial\eta_1}\right]_{x_1=0}^{L_1}\mathrm{d}^2\eta\,\mathrm{d}x_2+\int_{x_1=0}^{L_1}\int\int_{\eta}\left[-G_2\frac{\partial G_2^*}{\partial\eta_2}\right]_{x_2=0}^{L_2}\mathrm{d}^2\eta\,\mathrm{d}x_1,\end{aligned} \tag{120}$$

where the last two terms vanish due to periodic boundary conditions in the x_1 and x_2 directions, respectively.

The first integral in Eq. (120) vanishes at the limit $\eta_1 = 0$, due to symmetry: The function G_1 obeys the same symmetry properties (29) as $\hat{f}$, which is easily seen from the definition (59) of G_1. Therefore the product $G_1G_1^*$ is an *even* function with respect to η_2 at $\eta_1 = 0$,

and the expression $\eta_2 G_1 G_1^*$ is an *odd* function with respect to η_2. The integral of the second term $\eta_2 B_{01} G_1 G_1^*$ over the even interval $\eta = \pm\eta_{2,\max}$ therefore vanishes. The first term in the integral vanishes because of the symmetry (29) and the periodic boundary conditions in the x_1 direction, as is shown here:

$$\begin{aligned}
&\int\int_{\mathbf{x}}\int_{\eta_2=-\eta_{2,\max}}^{\eta_{2,\max}} \left[G_1^* \frac{\partial G_1}{\partial x_1}\right]_{\eta_1=0} \mathrm{d}\eta_2\, \mathrm{d}^2x = -\int\int_{\mathbf{x}}\int_{\eta_2=\eta_{2,\max}}^{-\eta_{2,\max}} \left[G_1^* \frac{\partial G_1}{\partial x_1}\right]_{\eta_1=0} \mathrm{d}\eta_2\, \mathrm{d}^2x \\
&= [\text{Change variable } \eta_2 \text{ to } -\eta_2] \\
&= +\int\int_{\mathbf{x}}\int_{\eta_2=-\eta_{2,\max}}^{\eta_{2,\max}} \left[G_1^*(x_1, x_2, 0, -\eta_2, t) \frac{\partial}{\partial x_1} G_1(x_1, x_2, 0, -\eta_2, t)\right] \mathrm{d}\eta_2\, \mathrm{d}^2x \\
&= [\text{Use the symmerty (29)}] \\
&= \int\int_{\mathbf{x}}\int_{\eta_2=-\eta_{2,\max}}^{\eta_{2,\max}} \left[G_1(x_1, x_2, 0, \eta_2, t) \frac{\partial}{\partial x_1} G_1^*(x_1, x_2, 0, \eta_2, t)\right] \mathrm{d}\eta_2\, \mathrm{d}^2x \\
&= [\text{Integrate by parts in } x_1 \text{ direction}] \\
&= \int_{x_2=0}^{L_2}\int_{\eta_2=-\eta_{2,\max}}^{\eta_{2,\max}} \left[(G_1 G_1^*)_{x_1=0}^{L_1} - \int_{x_1=0}^{L_1} G_1^* \frac{\partial G_1}{\partial x_1}\, \mathrm{d}x_1\right]_{\eta_1=0} \mathrm{d}\eta_2\, \mathrm{d}x_2 \\
&= -\int\int_{\mathbf{x}}\int_{\eta_2=-\eta_{2,\max}}^{\eta_{2,\max}} \left[G_1^* \frac{\partial G_1}{\partial x_1}\right]_{\eta_1=0} \mathrm{d}\eta_2\, \mathrm{d}^2x. \qquad (121)
\end{aligned}$$

The same expression appears on the left-hand and right-hand sides with opposite signs; thus the expression must be equal to zero.

What remains of Eq. (120) is now, after reordering of the terms,

$$\begin{aligned}
\frac{\mathrm{d}\|\hat{f}\|^2}{\mathrm{d}t} = &\int_{x_2=0}^{L_2}\int_{\eta_2=-\eta_{2,\max}}^{\eta_{2,\max}} \mathrm{i}\left[\int_{x_1=0}^{L_1} G_1^*\left(\frac{\partial}{\partial x_1} - \mathrm{i}\eta_2 B_{01}\right) G_1 \mathrm{d}x_1\right]_{\eta_1=\eta_{1,\max}} \mathrm{d}\eta_2\, \mathrm{d}x_2 \\
&+ \int_{x_1=0}^{L_1}\int_{\eta_1=0}^{\eta_{1,\max}} \left\{\mathrm{i}\left[\int_{x_2=0}^{L_2} G_2^*\left(\frac{\partial}{\partial x_2} + \mathrm{i}\eta_1 B_{02}\right) G_2\, \mathrm{d}x_2\right]_{\eta_2=\eta_{2,\max}}\right. \\
&\left. - \mathrm{i}\left[\int_{x_2=0}^{L_2} G_2^*\left(\frac{\partial}{\partial x_2} + \mathrm{i}\eta_1 B_{02}\right) G_2\, \mathrm{d}x_2\right]_{\eta_2=-\eta_{2,\max}}\right\} \mathrm{d}\eta_2\, \mathrm{d}x_2. \qquad (122)
\end{aligned}$$

By using the Parseval relation for the Fourier series pairs (42)–(47),

$$\int_{x_1=0}^{L_1} G_1^* \Gamma_1 \mathrm{d}x_1 = L_1 \sum_{i_1=-\infty}^{\infty} \tilde{G}_{1,i_1}^* \tilde{\Gamma}_{1,i_1} = L_1 \sum_{i_1=-\infty}^{\infty} (\mathrm{F}_1 G_1)_{i_1}^* (\mathrm{F}_1 \Gamma_1)_{i_1} \qquad (123)$$

and

$$\int_{x_2=0}^{L_2} G_2^* \Gamma_2\, \mathrm{d}x_2 = L_2 \sum_{i_2=-\infty}^{\infty} \tilde{G}_{2,i_2}^* \tilde{\Gamma}_{2,i_2} = L_2 \sum_{i_2=-\infty}^{\infty} (\mathrm{F}_2 G_2)_{i_2}^* (\mathrm{F}_1 \Gamma_2)_{i_2}, \qquad (124)$$

where in Eq. (122)

$$\Gamma_1 = \left(\frac{\partial}{\partial x_1} - i\eta_2 B_{01}\right) G_1 \quad \text{and} \quad \Gamma_2 = \left(\frac{\partial}{\partial x_2} + i\eta_1 B_{02}\right) G_2, \qquad (125)$$

we have

$$\frac{\mathrm{d}\|\hat{f}\|^2}{\mathrm{d}t} = \int_{x_2=0}^{L_2}\int_{\eta_2=-\eta_{2,\max}}^{\eta_{2,\max}} \mathrm{i}\left[L_1 \sum_{i_1=-\infty}^{\infty} (\mathrm{F}_1 G_1)^*_{i_1}\big(\mathrm{i}k_{x_1} - \mathrm{i}\eta_2 B_{01}\big)(\mathrm{F}_1 G_1)_{i_1}\right]_{\eta_1=\eta_{1,\max}} \mathrm{d}\eta_2\,\mathrm{d}x_2$$
$$+ \int_{x_1=0}^{L_1}\int_{\eta_1=0}^{\eta_{1,\max}} \left\{\mathrm{i}\left[L_2 \sum_{i_2=-\infty}^{\infty} (\mathrm{F}_2 G_2)^*_{i_2}\big(\mathrm{i}k_{x_2} + \mathrm{i}\eta_1 B_{02}\big)(\mathrm{F}_2 G_2)_{i_2}\right]_{\eta_2=\eta_{2,\max}}\right.$$
$$\left. - \mathrm{i}\left[L_2 \sum_{i_2=-\infty}^{\infty} (\mathrm{F}_2 G_2)^*_{i_2}\big(\mathrm{i}k_{x_2} + \mathrm{i}\eta_1 B_{02}\big)(\mathrm{F}_2 G_2)_{i_2}\right]_{\eta_2=-\eta_{2,\max}}\right\} \mathrm{d}\eta_2\,\mathrm{d}x_2. \tag{126}$$

By applying the boundary conditions (63)–(65) we now have

$$\frac{\mathrm{d}\|\hat{f}\|^2}{\mathrm{d}t} = \int_{x_2=0}^{L_2}\int_{\eta_2=-\eta_{2,\max}}^{\eta_{2,\max}} \left[L_1 \sum_{i_1=-\infty}^{\infty} -(\mathrm{F}_1 G_1)^*_{i_1}\big(k_{x_1} - \eta_2 B_{01}\big)\right.$$
$$\left.\times H\big(k_{x_1} - \eta_2 B_{01}\big)(\mathrm{F}_1 G_1)_{i_1}\right]_{\eta_1=\eta_{1,\max}} \mathrm{d}\eta_2\,\mathrm{d}x_2$$
$$+ \int_{x_1=0}^{L_1}\int_{\eta_1=0}^{\eta_{1,\max}} \left\{\left[L_2 \sum_{i_2=-\infty}^{\infty} -(\mathrm{F}_2 G_2)^*_{i_2}\big(k_{x_2} + \eta_1 B_{02}\big)\right.\right.$$
$$\left.\times H\big(k_{x_2} + \eta_1 B_{02}\big)(\mathrm{F}_2 G_2)_{i_2}\right]_{\eta_2=\eta_{2,\max}}$$
$$\left. + \left[L_2 \sum_{i_2=-\infty}^{\infty} (\mathrm{F}_2 G_2)^*_{i_2}\big(k_{x_2} + \eta_1 B_{02}\big) H\big(-k_{x_2} - \eta_1 B_{02}\big)(\mathrm{F}_2 G_2)_{i_2}\right]_{\eta_2=-\eta_{2,\max}}\right\} \mathrm{d}\eta_2\,\mathrm{d}x_2, \tag{127}$$

where $k_{x_1} = 2\pi i_1/L_1$ and $k_{x_2} = 2\pi i_2/L_2$. The Heaviside function truncates the sums, and we finally have

$$\frac{\mathrm{d}\|\hat{f}\|^2}{\mathrm{d}t} = 2\pi \int_{x_2=0}^{L_2}\int_{\eta_2=-\eta_{2,\max}}^{\eta_{2,\max}} \left[\sum_{i_1 \geq L_1\eta_2 B_{01}/2\pi} -(i_1 - L_1\eta_2 B_{01}/2\pi)\big|(\mathrm{F}_1 G_1)_{i_1}\big|^2\right]_{\eta_1=\eta_{1,\max}} \mathrm{d}\eta_2\,\mathrm{d}x_2$$
$$+ 2\pi \int_{x_1=0}^{L_1}\int_{\eta_1=0}^{\eta_{1,\max}} \left\{\left[\sum_{i_2 \geq -L_2\eta_1 B_{02}/2\pi} -(i_2 + \eta_1 B_{02}/2\pi)\big|(\mathrm{F}_2 G_2)_{i_2}\big|^2\right]_{\eta_2=\eta_{2,\max}}\right.$$
$$\left. + \left[\sum_{i_2 \leq -L_2\eta_1 B_{02}/2\pi} (i_2 + L_2\eta_1 B_{02}/2\pi)\big|(\mathrm{F}_2 G_2)_{i_2}\big|^2\right]_{\eta_2=-\eta_{2,\max}}\right\} \mathrm{d}\eta_2\,\mathrm{d}x_2. \tag{128}$$

Each term in the sums is nonpositive. Therefore the energy norm is nonincreasing with time, and we conclude that the continuous problem with the given boundary conditions is well-posed.

ACKNOWLEDGMENTS

I want to thank Bertil Gustafsson at the Department of Scientific Computing, Uppsala University, and Bo Thidé at the Swedish Institute of Space Physics, Uppsala Division, for fruitful discussions and their useful advice during my work. Special thanks to Prof. Helmut Neunzert at the University of Kaiserslauten, Germany, who kindly sent me published and unpublished material on the Boltzmann equation from his research, and to Anders Tjulin at the Department of Astronomy and Space Physics, Uppsala University, who kindly helped me obtain numerical values from the WHAMP program.

This research was financially supported by the Swedish National Graduate School in Scientific Computing (NGSSC) and the Swedish National Sciences Research Council (NFR).

REFERENCES

1. T. P. Armstrong, R. C. Harding, G. Knorr, and D. Montgomery, Solution of Vlasov's equation by transform methods, *Methods Comput. Phys.* **9**, 29 (1970).
2. F. F. Chen, *Introduction to Plasma Physics and Controlled Fusion*, Vol. 1: *Plasma Physics*, 2nd ed. (Plenum, New York, 1984).
3. C. Z. Cheng, The integration of the Vlasov equation for a magnetized plasma, *J. Comput. Phys.* **24**, 348 (1977).
4. C. Z. Cheng and G. Knorr, The integration of the Vlasov equation in configuration space, *J. Comput. Phys.* **22**, 330 (1976).
5. F. W. Crawford and J. A. Tataronis, Absolute instabilities of perpendicularly propagating cyclotron harmonic plasma waves, *J. Appl. Phys.* **36**(9), 2930 (1965).
6. J. Denavit and W. L. Kruer, Comparison of numerical solutions of the Vlasov equation with particle simulations of collisionless plasmas, *Phys. Fluids* **14**(8), 1782 (1971).
7. B. Eliasson, Outflow boundary conditions for the Fourier transformed one-dimensional Vlasov–Poisson system, *J. Sci. Comput.* **16**(1), 1 (2001).
8. J. Feng and W. N. G. Hitchon, Self-consistent kinetic simulation of plasmas, *Phys. Rev. E* **61**, 3160 (1999).
9. F. Filbet, E. Sonnedrücker, and P. Bertrand, Conservative numerical schemes for the Vlasov equation, *J. Comput. Phys.* **172**, 166 (2001).
10. B. Gustafsson and P. Olsson, Fourth-order difference methods for hyperbolic IBVPs, *J. Comput. Phys.* **117**, 300 (1995).
11. A. J. Klimas and W. M. Farrel, A splitting algorithm for Vlasov simulation with filamentation filtration, *J. Comput. Phys.* **110**, 150 (1994).
12. A. J. Klimas, A method for overcoming the velocity space filamentation problem in collisionless plasma model solutions, *J. Comput. Phys.* **68**, 202 (1987).
13. S. K. Lele, Compact finite difference schemes with spectral-like resolution, *J. Comput. Phys.* **103**, 16 (1992).
14. T. B. Leyser, Stimulated electromagnetic emission in high-frequency electromagnetic pumping of the ionospheric plasma, *Space Sci. Rev.* **98**, 223 (2001).
15. C.-H. Lin, J. K. Chao, and C. Z. Cheng, One-demensional Vlasov simulations of Langmuir solitons, *Phys. Plasmas* **2**, 4195 (1995).
16. G. Manfredi, Long-time behaviour of nonlinear Landau damping, *Phys. Rev. Lett.* **79**, 2815 (1997).
17. H. Neunzert, *Verallgemeinerte Lösungen von Eigenwertproblemen, zugehörige Entwicklungsfragen und die Anwendung auf Gleichungen der Transporttheorie, Jül-816-MA* (Kernforschungsanlage Jülich, Zentralinstitut für Angewandte Mathematik, 1971).
18. H. Neunzert, *An Introduction to the Nonlinear Boltzmann–Vlasov Equation*, Preprint 28. Lectures given at the international summerschool "Kinetic Theories and Boltzmann Equation" of C.I.M.E. in Montecatini (Italy), June, 1981.
19. K. Rönnmark, *WHAMP: Waves in a Homogenous, Anisotropic, Multicomponent Plasma*, Report 179 (Kiruna Geophysical Institute, Kiruna, Sweden, 1982).
20. J. C. Strikwerda, *Finite Difference Schemes and Partial Differential Equations* (Wadsworth, Belmont, CA, 1989).